ApJS, 191:423–438, 2010 December
Preprint typeset using LaTeX style emulateapj v. 11/10/09

THE ATACAMA COSMOLOGY TELESCOPE (ACT): BEAM PROFILES AND FIRST SZ CLUSTER MAPS

A. D. Hincks[1], V. Acquaviva[2,3], P. A. R. Ade[4], P. Aguirre[5], M. Amiri[6], J. W. Appel[1], L. F. Barrientos[5], E. S. Battistelli[7,6], J. R. Bond[8], B. Brown[9], B. Burger[6], J. Chervenak[10], S. Das[11,1,3], M. J. Devlin[12], S. R. Dicker[12], W. B. Doriese[13], J. Dunkley[14,1,3], R. Dünner[5], T. Essinger-Hileman[1], R. P. Fisher[1], J. W. Fowler[1], A. Hajian[8,3,1], M. Halpern[6], M. Hasselfield[6], C. Hernández-Monteagudo[15], G. C. Hilton[13], M. Hilton[16,17], R. Hlozek[14], K. M. Huffenberger[18], D. H. Hughes[19], J. P. Hughes[2], L. Infante[5], K. D. Irwin[13], R. Jimenez[20], J. B. Juin[5], M. Kaul[12], J. Klein[12], A. Kosowsky[9], J. M. Lau[21,22,1], M. Limon[23,12,1], Y.-T. Lin[24,3,5], R. H. Lupton[3], T. A. Marriage[25,3], D. Marsden[12], K. Martocci[26,1], P. Mauskopf[4], F. Menanteau[2], K. Moodley[16,17], H. Moseley[10], C. B. Netterfield[27], M. D. Niemack[13,1], M. R. Nolta[8], L. A. Page[1], L. Parker[1], B. Partridge[28], H. Quintana[5], B. Reid[20,1], N. Sehgal[21], J. Sievers[8], D. N. Spergel[3], S. T. Staggs[1], O. Stryzak[1], D. S. Swetz[12,13], E. R. Switzer[26,1], R. Thornton[12,29], H. Trac[30,3], C. Tucker[4], L. Verde[20], R. Warne[16], G. Wilson[31], E. Wollack[10], and Y. Zhao[1]

[1] Joseph Henry Laboratories of Physics, Jadwin Hall, Princeton University, Princeton, NJ 08544, USA
[2] Department of Physics and Astronomy, Rutgers, The State University of New Jersey, Piscataway, NJ 08854-8019, USA
[3] Department of Astrophysical Sciences, Peyton Hall, Princeton University, Princeton, NJ 08544, USA
[4] School of Physics and Astronomy, Cardiff University, The Parade, Cardiff, Wales CF24 3AA, UK
[5] Departamento de Astronomía y Astrofísica, Facultad de Física, Pontificía Universidad Católica de Chile, Casilla 306, Santiago 22, Chile
[6] Department of Physics and Astronomy, University of British Columbia, Vancouver, BC V6T 1Z4, Canada
[7] Department of Physics, University of Rome "La Sapienza", Piazzale Aldo Moro 5, I-00185 Rome, Italy
[8] Canadian Institute for Theoretical Astrophysics, University of Toronto, Toronto, ON M5S 3H8, Canada
[9] Department of Physics and Astronomy, University of Pittsburgh, Pittsburgh, PA 15260, USA
[10] Code 553/665, NASA/Goddard Space Flight Center, Greenbelt, MD 20771, USA
[11] Berkeley Center for Cosmological Physics, LBL and Department of Physics, University of California, Berkeley, CA 94720, USA
[12] Department of Physics and Astronomy, University of Pennsylvania, 209 South 33rd Street, Philadelphia, PA 19104, USA
[13] NIST Quantum Devices Group, 325 Broadway Mailcode 817.03, Boulder, CO 80305, USA
[14] Department of Astrophysics, Oxford University, Oxford OX1 3RH, UK
[15] Max Planck Institut für Astrophysik, Postfach 1317, D-85741 Garching bei München, Germany
[16] Astrophysics and Cosmology Research Unit, School of Mathematical Sciences, University of KwaZulu-Natal, Durban, 4041, South Africa
[17] Centre for High Performance Computing, CSIR Campus, 15 Lower Hope Street, Rosebank, Cape Town, South Africa
[18] Department of Physics, University of Miami, Coral Gables, FL 33124, USA
[19] Instituto Nacional de Astrofísica, Óptica y Electrónica (INAOE), Tonantzintla, Puebla, Mexico
[20] ICREA & Institut de Ciencies del Cosmos (ICC), University of Barcelona, Barcelona 08028, Spain
[21] Kavli Institute for Particle Astrophysics and Cosmology, Stanford University, Stanford, CA 94305-4085, USA
[22] Department of Physics, Stanford University, Stanford, CA 94305-4085, USA
[23] Columbia Astrophysics Laboratory, 550 West 120th Street, Mail Code 5247, New York, NY 10027, USA
[24] Institute for the Physics and Mathematics of the Universe, The University of Tokyo, Kashiwa, Chiba 277-8568, Japan
[25] Department of Physics and Astronomy, The Johns Hopkins University, 3400 North Charles Street, Baltimore 21218-2686, MD
[26] Kavli Institute for Cosmological Physics, Laboratory for Astrophysics and Space Research, 5620 South Ellis Ave., Chicago, IL 60637, USA
[27] Department of Physics, University of Toronto, 60 Street George Street, Toronto, ON M5S 1A7, Canada
[28] Department of Physics and Astronomy, Haverford College, Haverford, PA 19041, USA
[29] Department of Physics, West Chester University of Pennsylvania, West Chester, PA 19383, USA
[30] Harvard-Smithsonian Center for Astrophysics, Harvard University, Cambridge, MA 02138, USA and
[31] Department of Astronomy, University of Massachusetts, Amherst, MA 01003, USA

Submitted 2009 June 19; accepted 2010 November 3; published 2010 December 2

ABSTRACT

The Atacama Cosmology Telescope (ACT) is currently observing the cosmic microwave background with arcminute resolution at 148 GHz, 218 GHz, and 277 GHz. In this paper, we present ACT's first results. Data have been analyzed using a maximum-likelihood map-making method which uses B-splines to model and remove the atmospheric signal. It has been used to make high-precision beam maps from which we determine the experiment's window functions. This beam information directly impacts all subsequent analyses of the data. We also used the method to map a sample of galaxy clusters via the Sunyaev-Zel'dovich (SZ) effect, and show five clusters previously detected with X-ray or SZ observations. We provide integrated Compton-y measurements for each cluster. Of particular interest is our detection of the $z = 0.44$ component of A3128 and our current non-detection of the low-redshift part, providing strong evidence that the further cluster is more massive as suggested by X-ray measurements. This is a compelling example of the redshift-independent mass selection of the SZ effect.

Subject headings: cosmic background radiation – cosmology: observations – galaxies: clusters: general – methods: data analysis

1. INTRODUCTION

A new generation of experiments is measuring the cosmic microwave background (CMB) at arcminute resolutions. Within the past year alone, results from the South Pole Telescope (Staniszewski et al. 2009), ACBAR (Reichardt et al. 2009a), AMiBA (Umetsu et al. 2009), APEX-SZ (Reichardt et al. 2009b), the Cosmic Background Imager (Sievers et al. 2009), the Sunyaev-Zel'dovich Array (Sharp et al. 2010), and QUaD (Friedman et al. 2009) have revealed the ~arcminute structure of the CMB with higher precision than ever. The angular power spectrum of temperature fluctuations at these scales ($\ell \gtrsim 1000$) will further constrain models of the early universe. Furthermore, secondary features such as the Sunyaev-Zel'dovich (SZ) effect and gravitational lensing probe the growth of structure.

With its first science release, the Atacama Cosmology Telescope (ACT) now adds to these endeavors. A 6 m, off-axis Gregorian telescope, it was commissioned on Cerro Toco in northern Chile in 2007 October. Its current receiver is the Millimeter Bolometer Array Camera (MBAC), containing three 32×32 arrays of transition edge sensor (TES) bolometers observing at central frequencies of 148 GHz, 218 GHz, and 277 GHz, with beam full-widths at half-maxima (FWHM) of 1.′37, 1.′01, and 0.′91, respectively (see Section 3.2, below). It has operated for three seasons and is currently in its fourth season. In 2007 one month of science observations was made using only the 148 GHz array. The other two frequencies were added for the 2008 season, which lasted about 3.5 months. The telescope optical design is described in Fowler et al. (2007). Hincks et al. (2008) and Switzer et al. (2008) report on the telescope performance and provide an overview of hardware and software systems. The MBAC design and details of TES detector properties and readout are in Niemack (2006), Marriage et al. (2006), Battistelli et al. (2008), Niemack et al. (2008), Swetz et al. (2008), Thornton et al. (2008), and Zhao et al. (2008).[32]

ACT is located at one of the premier sites for millimeter astronomy because of the high altitude (5200 m) and the dry atmosphere. The precipitable water vapor (PWV) had a median value of 0.56 mm during the nights of our 2008 season. Nevertheless, atmospheric emission remains the largest signal external to the receiver in our raw data, a reality for any ground-based millimeter-wave telescope. The atmospheric power dominates only at low temporal frequencies and this is the main reason we observe while scanning our telescope in azimuth. Though much of the atmospheric power is below the frequency of our 0.0978 Hz scans, on typical nights the atmosphere dominates the detector noise up to about 2 Hz.

In this paper we present a map-making method designed to model and remove the atmospheric signal in a manner which is unbiased with respect to the celestial signal. The method—which is independent of the map-making pipeline used for most other ACT analysis—currently produces its best results on small scales ($\lesssim 1^\circ$), so it is well-suited to making maps of objects with small angular sizes. One of the most useful applications has been the study of our instrumental beam with high signal-to-noise maps of planets. The beam profile affects all aspects of data analysis, including calibration, and we provide the beam characteristics in this paper. Additionally, we present new SZ measurements of five known clusters.

We proceed as follows: In Section 2 we introduce the map-making method, showing both the theory and some qualitative properties; Section 3 describes how we analyzed our beams, and presents the key measured parameters along with beam maps and radial profiles; window functions are derived in Section 4; Section 5 shows a selection of clusters imaged with the mapper; and we conclude in Section 6.

[32] Reprints of all the references in this paragraph may freely be downloaded from: http://www.physics.princeton.edu/act/papers.html.

2. THE COTTINGHAM MAPPING METHOD

In this section, we present a technique for removing the atmospheric power first described by Cottingham (1987) and used by Meyer et al. (1991), Boughn et al. (1992), and Ganga et al. (1993). The temporal variations in atmospheric signals are modeled using B-splines, a class of functions ideal for interpolation, discussed more below. The technique computes maximum-likelihood estimates of both the celestial and the atmospheric signals, using all available detectors in a single frequency band. We refer to it hereafter as the Cottingham method.

In the following subsections, we give a mathematical description of the Cottingham method (Section 2.1), followed by a discussion of its benefits and a comparison to the "destriping" method developed for *Planck*, which has close similarities (Section 2.2). Our approach for including the effects of spatial variability across the detector arrays is in Section 2.3. We discuss the use of B-splines in Section 2.4, and finish by outlining our implementation of the method (Section 2.5) and map-making steps (Section 2.6).

2.1. *The Algorithm*

The measured timestream d is modeled as a celestial signal plus an atmospheric component:

$$d = \mathbf{P}m + \mathbf{B}\boldsymbol{\alpha} + n, \tag{1}$$

where the pointing matrix $\mathbf{P}$ projects the celestial map m into the timestream, $\mathbf{B}$ is a matrix of basis functions with amplitudes $\boldsymbol{\alpha}$ which model the temporal variation of atmospheric power, and n is the noise. The timestream of measurements d may be a concatenation of multiple detectors if they have been properly treated for relative gain differences. Throughout this paper, this is the case: all working detectors from one frequency band are processed simultaneously.

We seek $\widetilde{\boldsymbol{\alpha}}$ and $\widetilde{m}$, estimates of the atmospheric amplitudes and the celestial map, respectively. Equation (1) prescribes that we subtract the atmospheric term to obtain the map estimate: $d' = d - \mathbf{B}\widetilde{\boldsymbol{\alpha}}$. The maximum-likelihood estimator is then given by the standard map-making equation (e.g., Tegmark 1997):

$$\widetilde{m} = \left(\mathbf{P}^T\mathbf{N}^{-1}\mathbf{P}\right)^{-1}\mathbf{P}^T\mathbf{N}^{-1}d' = \mathbf{\Pi}\left(d - \mathbf{B}\widetilde{\boldsymbol{\alpha}}\right), \tag{2}$$

where we call

$$\mathbf{\Pi} \equiv \left(\mathbf{P}^T\mathbf{N}^{-1}\mathbf{P}\right)^{-1}\mathbf{P}^T\mathbf{N}^{-1} \tag{3}$$

the *projection matrix* and $\mathbf{N} \equiv \langle nn^T \rangle$ is the noise covariance. The projection matrix $\mathbf{\Pi}$ is designed in such a way that the map estimate is not biased, in the sense that the error, $\widetilde{m} - m$, does not depend on m.

Given a set of basis functions $\mathbf{B}$, the Cottingham method minimizes the variance of the map pixel residuals with respect to the amplitudes $\widetilde{\boldsymbol{\alpha}}$. The residuals are the differences between the celestial signals measured in the timestream and the map estimate:

$$\begin{aligned}\Delta d &= d' - \mathbf{P}\widetilde{m} = d - \mathbf{B}\widetilde{\boldsymbol{\alpha}} - \mathbf{P}\mathbf{\Pi}\left(d - \mathbf{B}\widetilde{\boldsymbol{\alpha}}\right) \\ &= \left(\mathbf{1} - \mathbf{P}\mathbf{\Pi}\right)\left(d - \mathbf{B}\widetilde{\boldsymbol{\alpha}}\right),\end{aligned} \tag{4}$$

where $\mathbf{1}$ is the identity matrix. We differentiate χ^2:

$$\frac{\partial \chi^2}{\partial \widetilde{\boldsymbol{\alpha}}} = \frac{\partial}{\partial \widetilde{\boldsymbol{\alpha}}} \left(\Delta d^T \mathbf{N}^{-1} \Delta d\right)$$
$$= -2\mathbf{B}^T (\mathbf{1} - \mathbf{P\Pi})^T \mathbf{N}^{-1} (\mathbf{1} - \mathbf{P\Pi}) \left(d - \mathbf{B}\widetilde{\boldsymbol{\alpha}}\right)$$
$$= -2\mathbf{B}^T \mathbf{N}^{-1} (\mathbf{1} - \mathbf{P\Pi}) \left(d - \mathbf{B}\widetilde{\boldsymbol{\alpha}}\right). \quad (5)$$

The last equality can be obtained by expanding $\mathbf{\Pi}$ to its constituent elements (cf. Equation (3)) and simplifying. If we define the following:

$$\mathbf{\Xi} \equiv \mathbf{B}^T \mathbf{N}^{-1} (\mathbf{1} - \mathbf{P\Pi}), \quad \mathbf{\Theta} \equiv \mathbf{\Xi B}, \quad \boldsymbol{\phi} \equiv \mathbf{\Xi} d, \quad (6)$$

then when we set the derivative in Equation (5) to zero, we have the simple expression:

$$\mathbf{\Theta}\widetilde{\boldsymbol{\alpha}} = \boldsymbol{\phi}. \quad (7)$$

This is a linear equation which is straightforward to solve for the atmospheric basis function amplitude estimates $\widetilde{\boldsymbol{\alpha}}$. These can then be used in Equation (2) to estimate the map. In fact, both $\widetilde{\boldsymbol{\alpha}}$ and $\widetilde{m}$ are the maximum-likelihood estimators of the atmosphere and celestial map, respectively, for a given set of basis functions $\mathbf{B}$. We show this explicitly in Appendix A.

There is an arbitrary overall offset to the computed $\mathbf{B}\widetilde{\boldsymbol{\alpha}}$ which must be estimated to remove the background from maps. We return to this point in Section 2.6.

2.2. *Discussion*

The chief strength of the Cottingham method is that it estimates the atmospheric power in a way that is unbiased with respect to the map estimate itself. This important but subtle point is encapsulated in the term $(\mathbf{1} - \mathbf{P\Pi})$ in Equation (5), whose effect is to project out the map estimate from the data. Therefore, the solution to Equation (7) is not sensitive to the estimated celestial temperature, but only to a time-varying term which is represented by the atmospheric estimate $\mathbf{B}\widetilde{\boldsymbol{\alpha}}$. This should be contrasted with high-pass filtering or fitting a slowly-varying function to the timestream to remove low-frequency power. Such approaches require masking of high signal-to-noise celestial objects (such as planets or clusters) and/or multiple iterations to prevent corruption of the maps. Simulations are required to understand the effects of these time-domain filters on the final maps.

The Cottingham method has close similarities to the "destriping" technique developed in particular for *Planck* analysis (Delabrouille 1998; Burigana et al. 1999; Maino et al. 2002). In fact, the linear algebra presented in Section 2.1 is identical to some versions of destriping (e.g., Keihänen et al. 2004). The destriping techniques are intended primarily to remove $1/f$ instrumental noise—thus, for example, Keihänen et al. (2005) impose a prior on the estimate $\mathbf{B}\widetilde{\boldsymbol{\alpha}}$ based on detector noise. Sutton et al. (2009) also consider the effects of imposing a prior on the atmospheric noise. On the other hand, we use the Cottingham method to remove atmospheric power with a flat prior. A distinct feature of our method is that we process multiple detectors simultaneously since the atmospheric signal is common across detectors (see, however, Section 2.3). Further, our approach differs in that it uses B-splines as the basis for modeling the atmosphere (Section 2.4).

2.3. *Spatial Structure in the Atmosphere*

The Cottingham method as presented thus far assumes that the atmospheric signal $\mathbf{B}\boldsymbol{\alpha}$ is common among all the detectors. In fact, we know that there is also spatial structure in the atmosphere, meaning that in principle, each detector might see a different atmospheric signal. In practice, the finite telescope beam sets a lower limit on the spatial scale. We find that the atmospheric signal is coherent across a quarter to a third of the array, or about 5–7′. For reference, our 148 GHz channel, which has a 1.′37 FWHM in the far-field (Section 3.2), is sensitive to an angular size of approximately 10′ at a 1 km distance, roughly the distance to a typical turbulence layer in the atmosphere when pointed at 50° in altitude (Pérez-Beaupuits et al. 2005).

To account for this, we divide the 32×32 detector array into nine square *sub-arrays* of roughly equal size and fit for nine separate temporal atmospheric signals $\mathbf{B}_s\boldsymbol{\alpha}_s$, with the subscript s denoting the sub-array. These can all be done simultaneously if we adapt Equation (1):

$$d = \mathbf{P}m + \mathbf{S}\begin{pmatrix} \mathbf{B}_1 & \mathbf{0} & \dots & \mathbf{0} \\ \mathbf{0} & \mathbf{B}_2 & \dots & \mathbf{0} \\ \vdots & \vdots & \ddots & \vdots \\ \mathbf{0} & \mathbf{0} & \dots & \mathbf{B}_9 \end{pmatrix}\begin{pmatrix} \boldsymbol{\alpha}_1 \\ \boldsymbol{\alpha}_2 \\ \vdots \\ \boldsymbol{\alpha}_9 \end{pmatrix} + \mathbf{N}$$
$$= \mathbf{P}m + \mathbf{SB}'\boldsymbol{\alpha}' + n, \quad (8)$$

where $\mathbf{S}$ is a book-keeping matrix that remembers from which sub-array each measurement in d came. The Cottingham method proceeds exactly as before, except that we change $\mathbf{B} \rightarrow \mathbf{SB}'$ and $\boldsymbol{\alpha} \rightarrow \boldsymbol{\alpha}'$.

2.4. *The B-spline as a Model of Atmospheric Signal*

We follow Cottingham (1987) in choosing cubic basis B-splines for the basis functions $\mathbf{B}$. B-splines are widely used in the field of geometrical modeling, and numerous textbooks cover them (e.g., Bojanov et al. 1993; de Boor 2001; Schumaker 2007); here we summarize basic properties. Basis B-splines are a basis of functions whose linear combination is called a B-spline. The basis B-splines are fully determined by a knot spacing τ_k and a polynomial order p; a B-spline is flexible on scales larger than τ_k, while on smaller scales it is relatively rigid. The basis B-splines $b_{j,p}(t)$ of order p are readily evaluated using the Cox–de Boor recursion on the polynomial order. For m knots $\{t_j\}$ with $j = 0$ to $m-1$:

$$b_{j,0}(t) = \begin{cases} 1 & \text{if } t_j \le t < t_{j+1} \\ 0 & \text{otherwise} \end{cases},$$
$$b_{j,p}(t) = \frac{t - t_j}{t_{j+p} - t_j} b_{j,p-1}(t) + \frac{t_{j+p+1} - t}{t_{j+p+1} - t_{j+1}} b_{j+1,p-1}(t), \quad (9)$$

with j values restricted so that $j + p + 1 < m - 1$. For m knot times, $m + p - 1$ basis B-splines cover the interval between the first and the last knot time. The individual basis B-splines $b_{j,p}(t)$ are compact functions, such that the B-spline receives support from no more than p of its bases at any point. For modeling the atmospheric signal, we always choose knots uniformly spaced in time and use $p = 3$ (cubic).

Due to their flexibility on large scales, B-splines are ideal for modeling the slowly varying atmospheric signal. The frequency f_k below which power will be removed is determined by the knot spacing τ_k. Empirically, we find:

$$f_k \approx 1/2\tau_k. \quad (10)$$

Figure 1 shows an example of atmospheric estimation using the Cottingham method. The B-spline knot-spacing is $\tau_k = 0.25$ s, chosen for this example because it has $f_k = 2$ Hz, the approximate frequency at which the atmospheric power meets the

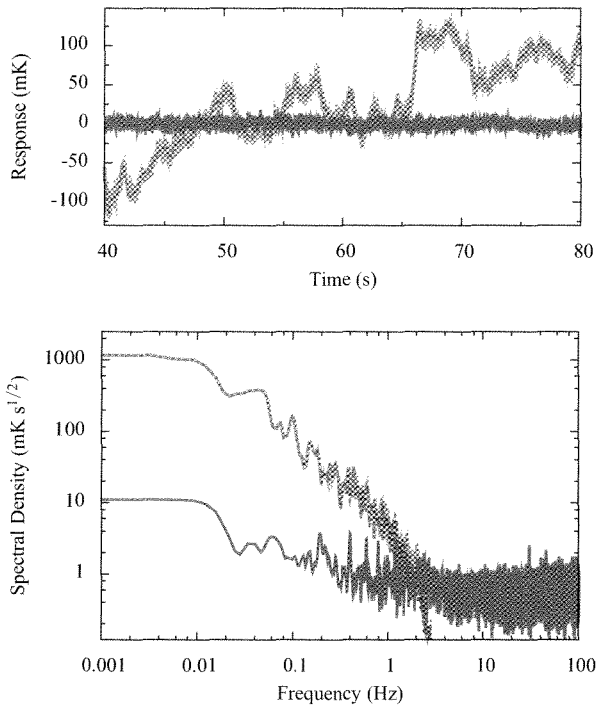

FIG. 1.— Example of the Cottingham method. The fit is done using 300 s of data from 605 148 GHz detectors. The PWV was 0.8 mm, about 0.25 mm higher than the median in 2008. The knot spacing is 0.25 s and the order is cubic. In both plots, the original signal is plotted with a solid, light line, the B-spline atmosphere model with a dashed line and the signal minus the model with a solid, dark line. Each plot has been smoothed with a five sample boxcar filter for readability. The temperature units are with respect to a Rayleigh-Jeans spectrum. Top: a portion of one of the detectors' timestreams. Bottom: the spectral densities for the same single detector. A Welch window was applied before computing the Fourier transform.

detector noise level. Longer knot spacings produce qualitatively similar results, except that they cut off at lower frequencies, as per Equation (10).

The Cottingham method is effective at suppressing atmospheric contamination, but some covariance between atmospheric and celestial map estimates remains. This is typically at harmonics of the scan frequency (≈ 0.1 Hz), as exemplified in the bottom panel of Figure 1. For this work we have used the white noise approximation for the detectors ($\mathbf{N} = 1$), which results in maps of bright sources which are clean down to the -40 dB level in most cases (Section 3). The small residual atmospheric-celestial covariance is manifested as striping along lines of constant altitude since with our 7° peak-to-peak, $1.^\circ5\,s^{-1}$ azimuthal scans (or $4.^\circ47$ at $0.^\circ958\,s^{-1}$ when projected on the sky at our observing altitude of $50.^\circ3$), the knot spacing ($\tau_k = 1.0$ s for beam maps (Section 3) and 0.5 s for cluster maps (Section 5)) corresponds to an angular scale smaller than the scan width. When noted, we fit straight lines to rows of pixels in the map, after masking out any bright source, and subtract them. We call this process, which takes place in the map domain, "stripe removal". In both our beam analysis and our cluster studies, we have done tests which show that the bias introduced by this process is not significant—see Section 3.2 and Section 5.3. Nevertheless, future extensions of the Cottingham method would benefit from the full treatment of the noise covariance.

2.5. *Implementation*

Before making maps with the Cottingham method, some preprocessing must be done. The data from all detectors, which are sampled at 400 Hz, are divided into fifteen-minute time-ordered data (TOD) files and the preprocessing is performed on each individual TOD—a future paper will describe the steps which we only summarize here. The data acquisition electronics' digital anti-aliasing filter as well as measured detector time constants are deconvolved from the raw data. Low frequency signal due to cryogenic temperature drifts is measured with dark detectors (i.e., detectors uncoupled to sky signal) and removed from signal detectors; a sine wave with period 10.23 s is also fit to each timestream and removed to reduce scan-synchronous contamination. Calibration to units of power uses nightly load curves obtained by sweeping through detector bias voltages and measuring the response. Relative gain imprecisions are removed by using the large atmospheric signal itself to flat field the detectors (e.g., Kuo et al. 2004); this is done independently in each of the nine sub-arrays (see Section 2.3). Finally, calibration to temperature units uses measurements of Uranus, for which we use a brightness temperature of 112 K with 6% uncertainty (Griffin & Orton 1993; Marten et al. 2005; Kramer et al. 2008). (The beam maps require no calibration to temperature—in fact, the temperature calibration is obtained from them.) The timestreams require no further preprocessing.

To improve the speed of the Cottingham algorithm, we exploit the fact that the map pixelization used for calculating the atmospheric signal (Equations (5)–(7)) need not be the same as the map-making pixelization. In general we only use a selection of the possible pixels on the map; additionally, we down-sample the number of hits in each pixel. We call the former "pixel down-sampling" and denote the fraction of retained pixels n_p; the latter we term "hit down-sampling" and denote the fraction of retained hits n_h. Consequently, the fraction of total available data used is $n_p \times n_h$. Each of these down-samplings is done in an even manner such that all working detectors are used, and also such that no large gaps exist in the remaining timestream.

We have specified four parameters for the Cottingham method: the knot-spacing τ_k, the pixel size ξ, the pixel down-sampling fraction, n_p, and the hit down-sampling fraction, n_h. Of these, we always choose $\xi = 18''$ (about 1/3 the 277 GHz beam size).

To evaluate the effect of varying the other three variables, we define a figure of merit which compares the average detector spectral density below 1 Hz to the white noise level, calculated in the range 5–25 Hz:

$$L \equiv \frac{1}{N_d}\sum_i^{N_d}\left[\frac{\int_{0\,\mathrm{Hz}}^{1\,\mathrm{Hz}} G_i(f)df}{\int_{0\,\mathrm{Hz}}^{1\,\mathrm{Hz}} df} \Big/ \frac{\int_{5\,\mathrm{Hz}}^{25\,\mathrm{Hz}} G_i(f)df}{\int_{5\,\mathrm{Hz}}^{25\,\mathrm{Hz}} df}\right], \qquad (11)$$

where the sum runs over the N_d detectors used for the Cottingham calculation and G_i is the spectral density of the ith detector *after* removing the estimated atmosphere signal. Figure 2 shows a plot of measured values of L for a selection of knot-spacings and pixel down-samplings. In our tests, we independently varied n_p and n_h, and found that the product $n_p \times n_h$, used in Figure 2, captures the important trend in the ranges of interest. As expected, shorter knot spacings remove more power: note however that only the $\tau_k = 0.5$ s and $\tau_k = 0.25$ s are capable of removing power up to the 1 Hz for which L is defined (cf. Equation (10)). Because the curves flatten out as $n_p n_h$ increases, at a certain point adding more data does not substantially improve the fit. This supports our conclusion that we only need to use a fraction of the data to estimate the atmosphere.

The timing data in the lower panel of Figure 2 were measured on a 64-bit Intel Xeon® 2.5 GHz processor. Computation time is dominated by the calculation of the variables in Equation (6).

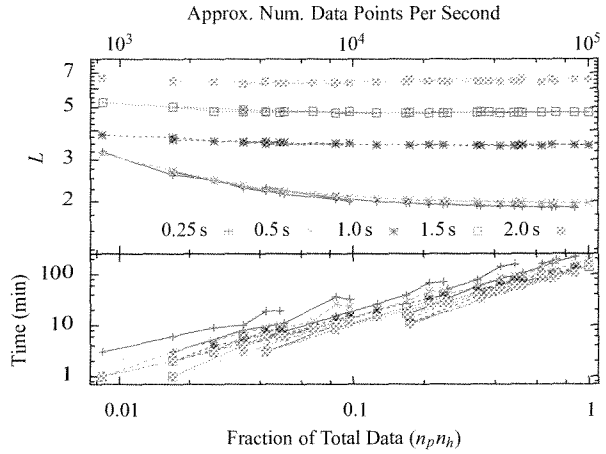

FIG. 2.— Top panel: the ratio L of low-frequency power to white noise after removing the atmospheric signal, as defined by Equation (11). All data points are from the same TOD using all working detectors; only the parameters τ_k, n_p and n_h (see the text) were varied to obtain each point. The x-axis is a product of the resamplings n_p and n_h, and the colors are different knot spacings τ_k as indicated in the plot key. Bottom panel: the computation time required for the data shown in the top panel. (The segmented lines are an artifact of how the data were recorded.) As the fraction $n_p n_h$ of total data used increases, the efficacy L of power removal flattens out and adding more data does not significantly improve the fit but only takes more computation time. In this example, there were ≈ 103000 possible map pixels with an average of 287 hits pixel^{-1}.

In general, these go linearly with the number of data points d and quadratically with the number of basis functions $\mathbf{B}$; in the case of B-splines, the compact support of the bases can be exploited so that the quadratic rate is subdominant to the linear, as the plot shows.

The number of basis B-splines is small enough that it is actually feasible to solve Equation (7) exactly. For most cases, however, the conjugate gradient method (e.g., Press et al. 1992, p. 83ff) is much faster and yields indistinguishable results. Therefore, we use the latter in our implementation.

2.6. *Map-making*

Once the atmospheric model $\mathbf{B}\boldsymbol{\alpha}$ has been calculated for a TOD with the Cottingham method, we create its celestial map. Maps are made in $(\Delta a,\ \Delta A\cos(a))$ coordinates, where Δa and ΔA are the distances from the altitude and azimuth of the map center.[33] We use a pixel size of 10.″6 per side, about 20% the size of the 277 GHz beam; note that this is different from the pixel size ξ used for calculating the atmosphere (Section 2.5). In this paper, the region of sky for which the atmospheric model is calculated is much wider in the azimuth than in altitude, since the telescope scans—4.°47 along the $\Delta A\cos(a)$ axis—are much wider than the distance the sky rotates along the Δa axis as the object of interest passes through the field of view. However, all of the maps we present are cropped to disks with 1:1 aspect ratios, centered on the objects being mapped.

We make the white noise approximation for each detector and weight it by the inverse of its variance in the map estimate. The detector variances are obtained iteratively: we make a map with equal detector weights and measure the variances of individual detector maps against the total map, remake the map with the new variances and repeat until the total map variance converges. The atmosphere estimates returned by the Cottingham method have arbitrary offsets, which can be different for the nine subarrays we use (see Section 2.3). Thus, in the same iterative process, we also fit for the sub-array offsets and remove them when coadding detectors.

Coaddition of TOD maps is done after all of the steps described above. The inverse variance of each map (calculated after masking bright point sources or clusters) is used as its median weight, and the relative weights of its pixels are given by the number of hits per pixel.

Finally, we mention that the software used for the results in this paper has a completely independent pipeline from our main map-making software which solves for the full survey area coverage. It has been especially useful for studying and optimizing the signal extraction in small, targeted regions, and has provided important double-checks for our other pipeline.

3. BEAM MAPS AND PROPERTIES

Understanding the telescope beams, or point-spread functions, is of primary importance for the interpretation of our maps since they determine the relative response of the instrument to different scales on the sky and are central to calibration. For ACT's measurement of angular power spectra, the Legendre transform of our measured beam profile, called a window function, determines the response of the instrument as a function of angular scale.

Planets are excellent sources for measuring the telescope's beam because they are nearly point sources and are brighter than almost any other celestial object. The best candidates for ACT are Saturn and Mars; of the rest, Jupiter is too bright and saturates the detectors, Venus is available too near to sunrise or sunset when the telescope is thermally settling, and the others are too dim for exploring the far sidelobes of the beam. (However, Uranus is useful as a calibrator—see Section 2.5.) The beam maps presented in this section are from observations of Saturn, which was available from early November through December of 2008. The possible concern of detector non-linearities when observing Saturn is obviated by the fact that atmospheric fluctuations, which are of the same order of magnitude in brightness as Saturn, are found to produce linear detector responses.

3.1. *Data Reduction*

Maps were made for each night-time TOD of Saturn, using the Cottingham method with $\tau_k = 1$ s, $n_p = 0.32$ and $n_h = 0.36$. We had more TODs than were needed to make low-noise beam maps, and we excluded about 1/3 of the maps which had higher residual background contamination, manifested by beam profiles that significantly diverged from those of the cleaner maps. The map sizes and number of TODs per frequency band are shown in Table 1.

In the analysis of Section 3.2, below, we sometimes compare unprocessed maps to stripe-removed maps. Stripe-removed map have been treated as outlined in Section 2.4, while unprocessed maps have not been altered after map-making except for the subtraction of a background level. The planet is masked out before calculating the mean map value which estimates this level. The mask sizes for the three arrays, whether used for stripe removal or background estimation, are listed in Table 1.

In each frequency band, the selected TOD beam maps were coadded. Weights were determined from the rms of the mean background level, calculated outside the mask radius. Relative pointing of individual detectors was measured to sub-arcsecond precision using the ensemble of Saturn observations. The overall telescope pointing was determined from each planet observation prior to map-making and used to center each TOD map, so recentering of the maps was unnecessary before coaddition.

[33] This is a very good approximation to the Gnomonic projection for the small map sizes we use.

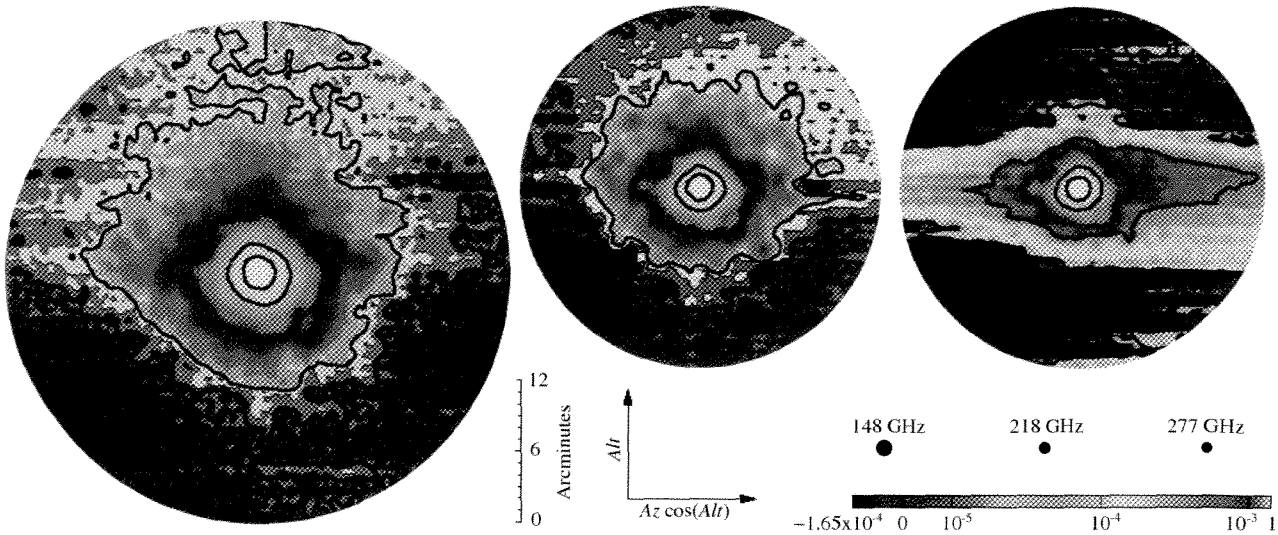

FIG. 3.— Beam maps for the three frequency bands: from left to right, 148 GHz, 218 GHz and 277 GHz. The maps are from coadded observations on 11–15 nights (see Table 1) and have radii of 21′ (148 GHz) and 15′ (218 GHz and 277 GHz). Maps are normalized to unity and contours are in decrements of −10 dB. A histogram equalized color scale is used to highlight the fact that we have made < −40 dB beam measurements of our 148 GHz and 218 GHz bands. (Negative values are due to noise about the mean background level.) Even in the inferior 277 GHz map, striping is still below −20 dB. The disks above the color bar show the sizes of the beam FWHM for each band (see Table 1). A Gaussian smoothing kernel with $\sigma = 0.'54$ has been applied to highlight large-scale structure; smoothing is not otherwise performed in the analysis. No stripe removal has been done on these maps.

3.2. *Beam Measurements*

Figure 3 shows coadded beam maps for the three arrays using a color scale which highlights the features in the sidelobes. The 148 GHz and 218 GHz maps have striking similarities, most notably along the altitude (or vertical) direction where both exhibit more power near the top of the map. This is due to the off-axis design of the telescope (see Fowler et al. 2007): since the 148 GHz and 218 GHz arrays sit at about the same vertical offset from the center of the focal plane, their resemblance along this axis is expected. Note that we recover structure in these map at a < −40 dB level. The 277 GHz map is clearly inferior, showing residual striping in the scan direction, although this occurs below −20 dB. We believe that this is from a combination of the brighter atmosphere at 277 GHz, as well as detector noise correlation induced by large optical loads (such as Saturn), which we are still investigating. Nonetheless we are still able to measure the 277 GHz solid angle to about 6% (see below), and work is underway to improve it.

For the 148 GHz and 218 GHz arrays, we do our beam analysis on maps which have not had stripe removal because this process removes the real vertical gradient from the maps (see Figure 3). Nonetheless, the solid angles (see below) from stripe-removed maps are within 1σ of the values from unprocessed maps. On the other hand, the larger residual striping in the 277 GHz maps necessitates the use of stripe-removed maps.

The beam center is characterized by fitting an elliptical Airy pattern—the function describing the beam of an optical system with a perfect aperture—to the top ∼3 dB of the beam map. This provides a measurement of the location of the beam center, its FWHM along the major and minor axes of the ellipse, and its orientation, which we define as the angle of the major axis from the line of zero altitude relative to the beam center. The uncertainties in these parameters are determined using the bootstrap method (Press et al. 1992, pp. 691ff) and give errors consistent with the standard deviation of values measured from the individual TOD maps. The FWHM and angles are listed in Table 1. They are included for reference but are not used in any analysis.

We denote the beam map by $B(\theta, \phi)$, where we use coordinates with radial distance θ from the beam center and polar angle ϕ. By definition, $B(0, \phi) = 1$. The symmetrized beam is averaged around the polar angle:

$$b^S(\theta) \equiv \frac{\int d\phi' B(\theta, \phi')}{\int d\phi'}. \quad (12)$$

TABLE 1
SUMMARY OF BEAM PARAMETERS

	148 GHz	218 GHz	277 GHz
Map properties (Section 3.1)			
No. of TODs	16	15	11
Stripe removal?	no	no	yes
Map radius (′)	21	15	15
Mask radius (′)[a]	18	9,11,13	6,8,10,12
Beam centers (Section 3.2)			
Major FWHM (′)	1.406 ± 0.003	1.006 ± 0.01	0.94 ± 0.02
Minor FWHM (′)	1.344 ± 0.002	1.001 ± 0.003	0.88 ± 0.02
Axis angle (°)	62 ± 2	137 ± 9	98 ± 13
θ_W wing fits (Section 3.2)			
Fit start, θ_1 (′)	7	5	4.5
Fit end, θ_2 (′)[b]	13	7–11	6–10
Best-fit θ_W (′)	0.526 ± 0.002	0.397 ± 0.01	0.46 ± 0.04
Solid angles (Section 3.2)			
Solid angle (nsr)	218.2 ± 4	118.2 ± 3	104.2 ± 6
Percent interpolated	2.8	4.3	7.2
Beam fits (Section 4.1)			
θ_0 (′)	0.2137	0.1562	0.1367

NOTE. — See the text for definitions of these parameters and how they are measured. Values for the 148 GHz and 218 GHz bands are obtained from the coadded, unprocessed maps whereas the 277 GHz values are average values from stripe-removed maps with the mask sizes indicated in the table.

[a] The 218 GHz and 277 GHz beam properties are averaged from the results at these mask radii—see the text.

[b] The fit ranges for the 218 GHz and 277 GHz band are varied along with the mask radii so that θ_2 is never larger than the mask—see text.

Another quantity of interest is the accumulated solid angle, which measures the total normalized power within a given radius:

$$\Omega(\theta) = \int_0^{2\pi} d\phi' \int_0^{\theta} \theta' d\theta' B(\theta', \phi'). \quad (13)$$

The beam solid angle is $\Omega_A \equiv \Omega(\theta = \pi)$.

Figure 4 shows measured beam profiles and accumulated solid angles for the three arrays. We measure the beam profiles down to about −45 dB. If the beams exactly followed an Airy pattern, these data would account for 98% of the solid angle. Since systematic effects could corrupt our maps at the largest radii, we seek a way to robustly estimate the last few percent of the solid angle on each beam. The method is to extrapolate the data with a fit to the asymptotic expression for the Airy pattern:

$$b^S(\theta \gg \theta_F) = \left(\frac{\theta_W}{\theta}\right)^3, \quad (14)$$

where θ_F is the beam FWHM and θ_W defines the wing scale. Equation (14) is good to better than 1% beyond about $5\theta_F$ (Schroeder 2000, Section 10.2b).[34] Knowledge of θ_W allows us to infer the amount of unaccounted solid angle beyond the map boundary. A simple integration shows that the solid angle beyond a radius θ_b is:

$$\Omega_W(\theta > \theta_b) = 2\pi \frac{\theta_W^3}{\theta_b}. \quad (15)$$

We can also use this expression to estimate the amount of true beam power which was "mistakenly" included in the measurement of the background level outside the mask radius and subtracted from the map. In our analysis of the beam profiles and solid angles (including those displayed in Figure 4), we use the fits of θ_W to calculate this missing power and add it back into the map. A new θ_W is then calculated from the corrected map; after two such iterations the θ_W fit converges.

Figure 4 includes over-plots of the wing estimates from the best-fit values of θ_W on unprocessed maps. We denote the radii between which the fits were performed as θ_1–θ_2, and choose $\theta_1 \approx 5\theta_F$ for each array. For 148 GHz, we obtain good fits for any choice of θ_2 up to 13′, or about the −40 dB level in the profile. Thus, we use $\theta_2 = 13'$, for which we fit with χ^2 of 40 for 35 degrees of freedom. The fits to the other profiles are not as robust: 218 GHz has a reduced-χ^2 of 2.8 for $\theta_2 = 7'$ and 277 GHz has reduced-χ^2 of 25 for $\theta_2 = 6'$. Larger θ_2 gave poorer fits. Consequently, for these profiles we calculate θ_W at different mask sizes, as indicated in Table 1. At each mask size we varied θ_2 in 2′ increments, always keeping it lower than the mask size. The average value from the whole ensemble of fits gives us θ_W and we take its standard error as the uncertainty. Although Equation (14) may be too simple a model for these profiles, contributions to the solid angle at these radii are only a few percent of the total solid angle, which has an uncertainty dominated by the contribution of the beam at radii less than θ_2—see below. The values of θ_W for all three beam profiles are listed in Table 1.

Our θ_W fits allow us to calculate precise solid angles. At radii smaller than θ_2, we integrate the normalized power in the map (cf. Equation (13)). Beyond θ_2, we use Equation (15) to extrapolate the remaining solid angle. (In the case of the 218 GHz and 277 GHz solid angles, we use the smallest θ_2 and the largest mask size in the ranges shown in Table 1. Other choices from these ranges do not significantly alter the results.) Finally, in the approximation that Saturn is a solid disk, it adds half of its solid angle Ω_S to the measured instrument solid angle—this is shown in Appendix B. Thus, the total solid angle is:

$$\Omega_A = \Omega(\theta \le \theta_2) + \Omega_W(\theta > \theta_2) - \Omega_S/2. \quad (16)$$

During the period of our observations, Saturn subtended solid angles from 5.2 to 6.0 nanosteradians (nsr). We use the mean value of 5.6 nsr.

Determining the rest of the uncertainty in the solid angle is not straightforward since systematic errors dominate. For our total error, we add the estimated uncertainties of each of the terms on the right-hand side of Equation (16) in quadrature. The uncertainty from Saturn's solid angle we take to be 1 nsr, both because of its varying angular size and to account for any systematic error due to the disk approximation.[35] The uncertainty of Ω_W is derived from the error of the fitted θ_W. For $\Omega(\theta < \theta_2)$, which dominates, we estimate the error by looking at the distribution of values from the individual TOD maps which comprise the coadded map. We did this in two ways. First, we calculated the mean and standard deviation of the solid angles measured in each individual map. This also reassures us that the coaddition step does not introduce any systematic error through, for example, pointing misalignments or changes in telescope focus from night to night. Second, we used the bootstrap method to generate 1000 coadded maps with random subsets of individual maps and used this ensemble to estimate the 68th percentile (i.e., 1σ) of solid angles. These two error estimates were consistent with each other.

The solid angles and their uncertainties are reported in Table 1. The formal uncertainties have been doubled and we quote them as 1σ, in case there are systematic effects for which we have not accounted. In particular, the maps used for power spectrum estimation will come from an independent pipeline and will treat the instrumental response in slightly different ways—for example, by weighting detectors differently. We expect the beam uncertainties to decrease as our analysis evolves.

4. WINDOW FUNCTIONS

The statistics of the CMB are frequently characterized by an angular power spectrum C_ℓ:

$$\Delta T(\hat{n}) = \sum_{\ell,m} a_{\ell m} Y_{\ell m}(\hat{n}); \quad \langle a^*_{\ell' m'} a_{\ell m} \rangle = \delta_{\ell' \ell} \delta_{m' m} C_\ell, \quad (17)$$

where $\Delta T(\hat{n})$ is the CMB temperature at position $\hat{n}$ and $Y_{\ell m}$ is a spherical harmonic. In spherical harmonic space, the beam is encoded in a window function w_ℓ describing the response of the experiment to different multipoles ℓ, such that the total variance of a noiseless power spectrum is:

$$\mathrm{Var} = \sum_\ell \frac{2\ell + 1}{4\pi} C_\ell w_\ell. \quad (18)$$

In the case of a symmetric beam, the window function is the square of the Legendre transform of the beam radial profile (White & Srednicki 1995; Bond 1996):

[34] In full generality Equation (14) is also proportional to $\cos(\pi D\theta/\lambda - 3\pi/4)$, where D is the telescope aperture diameter and λ is the wavelength; we have smoothed over cosine cycles.

[35] The rings of Saturn add a layer of complication to its solid angle calculation, particularly since they have a different temperature than the disk. The ring inclination was low during our observations ($< 6°$) and we have estimated that their contribution is negligible within the error budget.

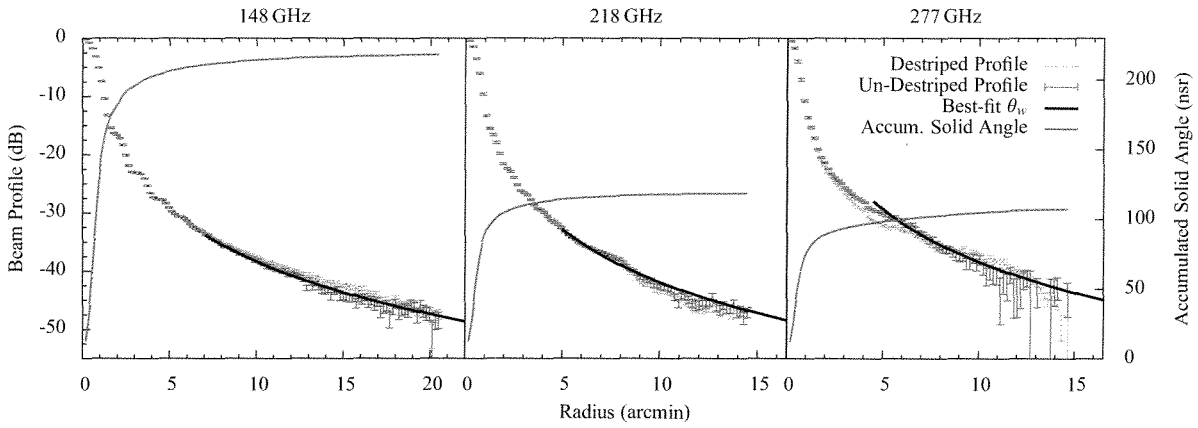

FIG. 4.— The beam profiles (Equation (12)) and accumulated solid angles (Equation (13)) for the three arrays, calculated from coadded maps (see text). The beam profiles are shown for both unprocessed maps, with dark errorbars, and stripe-removed maps, with light errorbars. Over-plotted on each profile is the best fit of θ_W (Equation (14)) to the unprocessed beam profiles. The error on the profiles are standard errors from the azimuthal average. The accumulated solid angles are from the unprocessed maps (without any solid angle extrapolation via Equation (15)) for 148 GHz and 218 GHz, and from the stripe-removed map for 277 GHz. Saturn is bright enough that the rms power from the CMB falls below all the points in these plots.

$$w_\ell = b_\ell^2; \quad b_\ell \equiv \frac{2\pi}{\Omega_A}\int b^S(\theta)P_\ell(\theta)d(\cos\theta). \tag{19}$$

4.1. *Basis Functions*

For calculation of the window function and its covariance we model each beam with a set of basis functions which is complete but not necessarily orthogonal:

$$b^S(\theta) = \sum_{n=0}^{n_{\max}} a_n b_n(\theta). \tag{20}$$

Because the beam is truncated by a cold Lyot stop (Fowler et al. 2007), its Fourier transform is compact on a disk, which suggests that a natural basis with which to decompose the Fourier transform of the beam image is the set of Zernike polynomials that form an orthonormal basis on the unit disk (Born & Wolf 1999). The Zernike polynomials, expressed in polar coordinates ρ and φ on the aperture plane, are:

$$V_n^m(\rho,\varphi) = R_n^m(\rho)e^{im\varphi}, \tag{21}$$

where m and n are integers such that $n \geq 0$, $n > |m|$ and $n - |m|$ is even. In the case of an azimuthally symmetric beam, we need only consider the $m = 0$ radial polynomials, which can be expressed in terms of Legendre polynomials, $P_n(x)$, as follows:

$$R_{2n}^0(\rho) = P_n(2\rho^2 - 1). \tag{22}$$

The radial Zernike polynomials have a convenient analytic form for their Fourier transform:

$$\tilde{R}_{2n}^0(\theta) = \int \rho d\rho e^{-i\rho\theta}R_{2n}^0(\rho) = (-1)^n J_{2n+1}(\theta)/\theta, \tag{23}$$

where J_n is a Bessel function of the first kind. Motivated by this, we adopt

$$b_n(\theta) = \left(\frac{\theta}{\theta_0}\right)^{-1} J_{2n+1}\left(\frac{\theta}{\theta_0}\right) \tag{24}$$

as our set of basis functions to fit the radial beam profile.[36] Here, we have introduced a fitting parameter, θ_0, to control the scale of the basis functions.

4.2. *Fitting Basis Functions to the Beam Profile*

Below θ_1 (cf. Table 1), we fit the bases b_n of Equation (24) to the measured beam profile, and beyond θ_1, we use the power law defined in Equation (14) with the parameters θ_W listed in Table 1. We assume vanishing covariance between the power law and the basis functions as they are fitted to independent sets of data points.

We employ a nonlinear, least-squares method to solve for the coefficients a_n and their covariance matrix $C_{mn}^{aa'}$. The algorithm uses a singular value decomposition to determine if the basis functions accurately characterize the data and also computes a goodness-of-fit statistic (Press et al. 1992, Section 15.4). As inputs to the fitting procedure we are required to specify the scale parameter, θ_0, and polynomial order, $n_{\max}$. We searched the $\{\theta_0, n_{\max}\}$ parameter space until a reasonable fit was obtained that kept $n_{\max}$ as small as possible. For all three bands, $n_{\max} = 13$ gives a reduced $\chi^2 \approx 1$. No singular values is found for any of the fits. The parameters θ_0 we use for each frequency band are listed in Table 1.

4.3. *Window Functions and Their Covariances*

Given the amplitudes a_n of the radial beam profile fitted to the basis functions and the covariance matrix $C_{mn}^{aa'}$ between the amplitudes a_m and a_n, the beam Legendre transform is:

$$b_\ell = \sum_{n=0}^{n_{\max}} a_n b_{\ell n}. \tag{25}$$

and the covariance matrix of the beam Legendre transforms b_ℓ and $b_{\ell'}$ is:

$$\Sigma_{\ell\ell'}^b = \sum_{m,n=0}^{n_{\max}} \frac{\partial b_\ell}{\partial a_m} C_{mn}^{aa'} \frac{\partial b_{\ell'}}{\partial a_n} \tag{26}$$

[36] It may be asked why the Airy pattern, which was somewhat suitable for the high-θ fit in Section 3.2, is not used here. We find that at low θ, it is a poor fit since the optics are more complicated than the perfect-aperture model assumed by the Airy pattern.

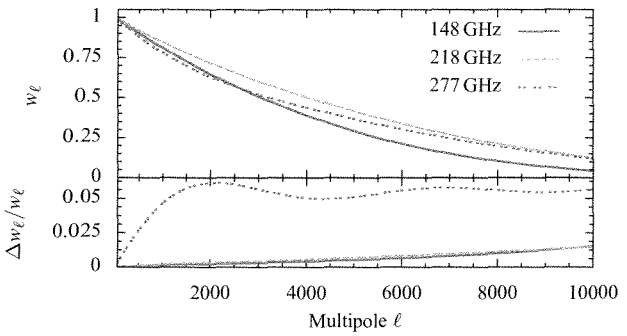

FIG. 5.— Normalized window functions (top) and diagonal errors (bottom) computed from the basis functions for each of the three frequency bands. The window functions have been normalized to unity at $\ell = 0$. In practice, the normalization will take place over the range of multipoles corresponding to the best calibration. Only statistical errors are shown.

and therefore the covariance for the window function is:

$$\Sigma^w_{\ell\ell'} = 4 w_\ell w_{\ell'} \Sigma^b_{\ell\ell'}. \quad (27)$$

In Figure 5 we show the window functions for each of the three frequency bands with diagonal error bars taken from the covariance matrix, $\Sigma^w_{\ell\ell'}$. We observe that the window function for each of the frequency bands has fallen to less than 15% of its maximum value at $\ell = 10000$. The statistical diagonal errors are at the 1.5%, 1.5%, and 6% levels for the 148 GHz, 218 GHz, and 277 GHz bands respectively, as shown in Figure 5. They are computed following Equation (17) of Page et al. (2003). The off-diagonal terms in the beam covariance matrix are comparable in magnitude to the diagonal terms. Singular value decompositions of $\Sigma^b_{\ell\ell'}$ yield only a handful of modes with singular values larger than 10^{-3} of the maximum values: five modes for 148 GHz, four for 218 GHz, and two for 277 GHz. Thus, the window function covariances can be expressed in a compact form which will be convenient for power spectrum analyses.

For 277 GHz we estimate a 10% systematic uncertainty from destriping. Another source of systematic error in the window functions arises from the beams not being perfectly symmetric. The symmetrized beam window function generally underestimates the power in the beam (e.g., Figure 23, Hinshaw et al. 2007). In practice, the scans in our survey field are cross-linked (see Section 5.1). Thus, given the spherical transform of a cross-linked beam map b_ℓ, the window function of relevance for the power spectrum calculation is:

$$w_\ell = \frac{1}{2\pi} \int_0^{2\pi} b(\boldsymbol{\ell}) b^*(\boldsymbol{\ell}) d\phi_\ell, \quad (28)$$

where ϕ_ℓ is the polar angle in spherical harmonic space. We computed the fractional difference between the window function derived from the Legendre transform of the symmetrized beam (shown in Figure 5) to that derived from an estimated two-dimensional, cross-linked beam map. For the latter, we rotated our Saturn beam map by a typical cross-linking angle of 60°, coadded it with the original, and evaluated Equation (28) on the transform of this synthetic map. The difference between the two was found to be at the 1% level for the 148 GHz and 218 GHz arrays, and at the 4% level for the 277 GHz array.

5. SZ GALAXY CLUSTERS

In addition to beam maps, the Cottingham method mapper has been used for making maps of SZ clusters. The maps and analysis presented in this section are the first results from ACT on SZ science. For this first overview, we include results from only the 148 GHz band, the most sensitive during our 2008 season. Of the five clusters presented in this paper, all of which were previously known, three are detected for the first time with the SZ effect.

5.1. *Data*

Table 2 lists the clusters studied in this paper, including information on the maps and a summary of the results of our analysis (Section 5.2, Section 5.3). Figure 6 shows the cluster maps and companion difference maps (see below).

Apart from planets, ACT has done no targeted observations of specific objects, so the cluster maps come from our regular survey data, which were taken at two different central azimuth pointings, one on the rising sky and the other on the setting sky. Therefore, the maps presented here are "cross-linked", i.e., they consist of data taken with two distinct angles between the azimuthal scan direction and the hour angle axis. The integration time is short, ranging from about 3 to 11 minutes—see Table 2.

The clusters were found in a full-survey 148 GHz map produced by our main map-maker. A Wiener filter was constructed using the polytropic model of Komatsu & Seljak (2001) as an SZ template, and included detector noise, CMB power and point source contributions in the noise model. Clusters were then identified from the filtered maps. We make two points about the clusters presented in this paper: first, although our template-based detection method has some built-in bias, the detections presented here are significant ($\geq 5\sigma$ in the filtered survey map); and second, we have only included a sample of our significant detections.

Cluster maps are made using the procedures outlined in Section 2.5 and Section 2.6. The knot spacing was $\tau_k = 0.5$ s and the downsampling fractions were $n_p \approx 0.42$ and $n_h \approx 0.40$. All maps are 0.°4 in diameter. Straight-line stripe removal (Section 2.6) has been performed, using a 6′ radius mask over the cluster decrement.

We have made companion "difference" maps for each cluster from the same data. For each of the rising and setting observations, a map made from the first half of the season's data is subtracted from the second half. The rising and setting difference maps are then coadded to produce the full, cross-linked coadded difference map—the same procedure used for the signal maps.

The map noise, listed in Table 2, is the rms of the map computed outside a 6′ mask and converted to an effective pixel size of 1 arcmin^2. By examining the power spectra of the maps we found that the rms values we quote are dominated by the white noise level and do not have significant contributions from residual low-frequency power.

5.2. *Cluster Profiles*

The cluster center positions are determined by finding the coldest point in the map smoothed with a 2′ FWHM Gaussian kernel. As a rough guide, we also quote the cluster depths, ΔT_{SZ}, from these smoothed maps in Table 2, but we stress that these values should not be used for quantitative analysis. All other cluster properties are measured from unsmoothed maps.

Figure 7 shows the clusters' radial temperature profiles, calculated by finding the mean map temperatures in 32″ wide annuli about the cluster centers listed in Table 2. The errorbars on the profiles plotted in Figure 7 are the standard errors of these mean values.

To highlight the size of the SZ decrements, 24 additional profiles are included in Figure 7, each from a map of a patch of the sky containing no clusters and processed in the same way as the cluster maps. Furthermore, to illustrate that the depth

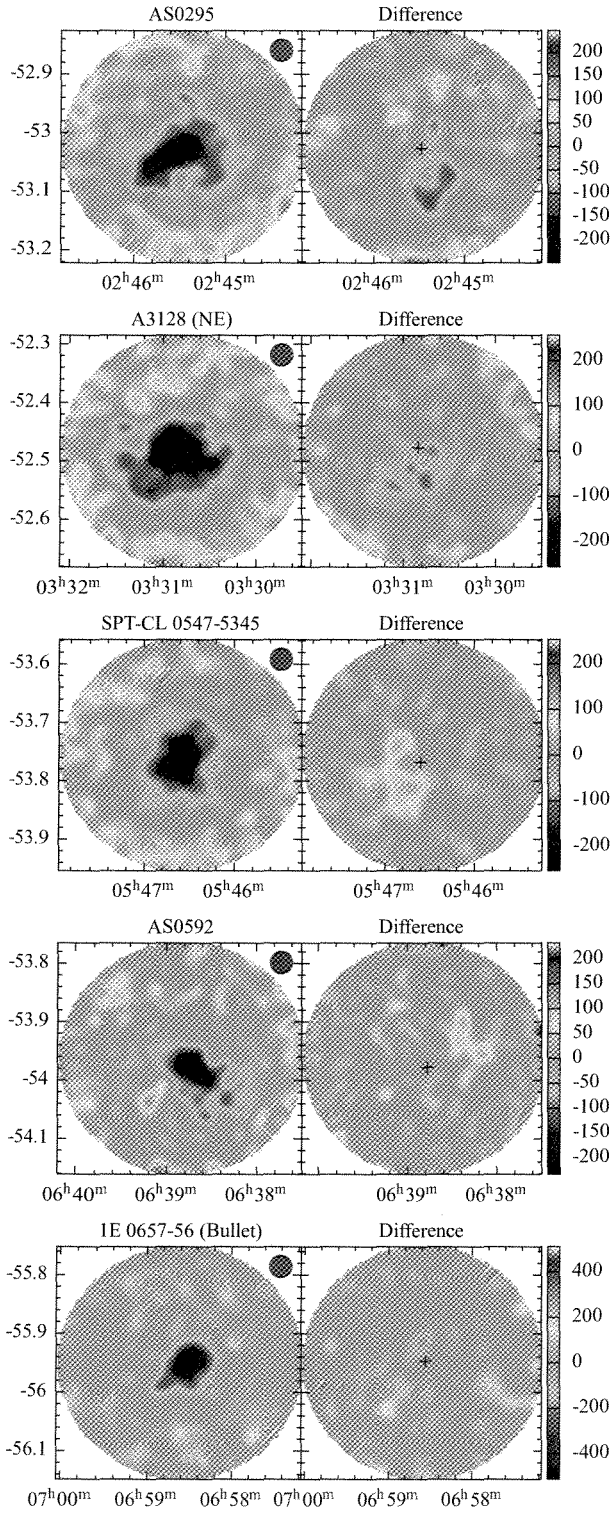

FIG. 6.— Cluster maps made using the Cottingham method at 148 GHz, paired with their difference maps (see Section 5.1). The coordinates are J2000 right ascension (hours) and declination (degrees). The color bars are μK (CMB); note that the scale is different for each cluster. The gray disk in the top corner of the the signal plots is 2′.43 in diameter, the FWHM size of the beam convolved with the Gaussian smoothing kernel which was applied to these images. In each difference plot, a cross shows the coordinates of the darkest spot in its corresponding signal map.

of the cluster profiles is much greater than the fluctuations in the primary CMB anisotropies, we created a large ensemble (1000) of noise-free, primary-anisotropy CMB simulations using a flat ΛCDM cosmology. These synthetic maps were made at the same size and resolution as our signal maps, and underwent the same stripe removal process. Figure 7 shows shaded areas which contain 68% and 95% of the simulated CMB radial profiles. The cluster profiles fall significantly below both the simulated CMB-only profiles and the profiles from blank CMB patches.

As a check that the choice of knot spacing ($\tau_k = 0.5$) is not creating a significant bias via covariance of the celestial signal with the low-frequency atmospheric estimate (see Section 2.4), we created maps with τ_k from 0.15 s to 1.5 s for ACT-CL J0245−5301 and ACT-CL J0638−5358. The temperature profiles for the latter are plotted in the middle panel of Figure 8. Even the shortest spacing does not produce a profile which is significantly different from the others. We conclude that the results are not biased by having knots of too high a frequency.

5.3. *Integrated Compton-y Values*

The SZ effect occurs when CMB photons inverse Compton-scatter off hot electrons in clusters of galaxies (Zeldovich & Sunyaev 1969; Sunyaev & Zel'dovich 1970). The imprint on the CMB is proportional to the integrated electron gas pressure:

$$\frac{\Delta T}{T_{\rm CMB}} = y f(x); \quad y \equiv \frac{k_B \sigma_T}{m_e c^2} \int dl\, n_e T_e, \tag{29}$$

where the integral is along the line of sight, m_e, n_e, and T_e are the electron mass, number density, and temperature, respectively, σ_T is the Thomson scattering cross-section, and the variable y is the Compton-y parameter. The function $f(x)$ encodes the dependence on frequency:

$$f(x) = \left[x \coth(x/2) - 4\right]\left[1 + \delta_{\rm SZ}(x, T_e)\right], \tag{30}$$

with $x \equiv h\nu / k_B T_{\rm CMB}$. The relativistic term $\delta_{\rm SZ}$ becomes important at higher temperatures (Rephaeli 1995), and is taken into account in our measurements below.

A robust measure of the SZ signal is the integrated Compton-y parameter, since it is model-independent and simply sums pixels in the maps (Verde et al. 2002; Benson et al. 2004):

$$Y(\theta) = \iint_{|\boldsymbol{\theta}'|<\theta} d\Omega_{\boldsymbol{\theta}'}\, y(\boldsymbol{\theta}'), \tag{31}$$

where $\boldsymbol{\theta}$ is the angular distance from the cluster center. We use steradians as the unit of solid angle, so Y is dimensionless. As an example, it is plotted for ACT-CL J0638−5358 in the lower panel of Figure 8. The values of Y at 2′, 4′, and 6′ are shown for each cluster in Table 2.

For clusters with measured temperatures (cf. Table 3), our Y values include the relativistic correction using the formulae from Nozawa et al. (2006). At 148 GHz, the corrections increase Y and, for the clusters in this paper, range from 4% (ACT-CL J0330−5228) to 7% (ACT-CL J0658−5556). Thus, the Y value quoted for ACT-CL J0546−5346, for which there is no measured temperature, is biased low, though we note that the relativistic corrections for the other clusters are smaller than the uncertainty of our measurements (see below).

There are two statistical sources of uncertainty in the measured Y values: instrumental and atmospheric noise in the map, and confusion of primary CMB anisotropies with the SZ signal.

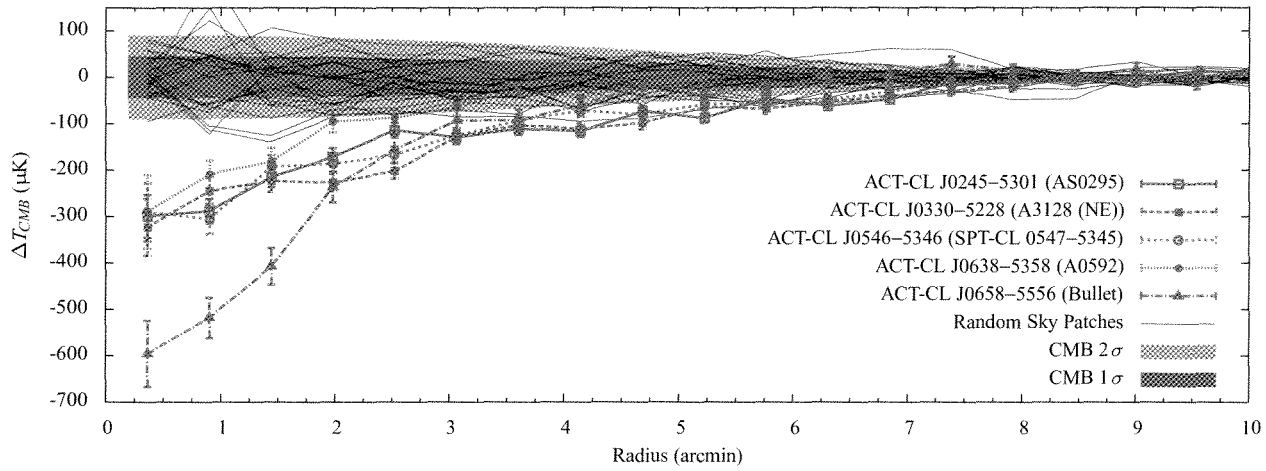

FIG. 7.— Radial cluster profiles, calculated by finding the mean temperature in the maps in 32″ wide annuli. For comparison, the radial profiles for the 24 maps of random patches of the sky, not containing clusters, are included; additionally, shaded areas show the range containing 68% and 95% of profiles from an ensemble of 1000 simulated, noise-free CMB patches (cf. Section 5.3). The locations of the profile centers are listed in Table 2. The 1.′4 FWHM beam has not been deconvolved from any of the profiles.

TABLE 2
SELECTION OF SZ CLUSTERS DETECTED BY ACT

ACT Descriptor	Catalog Name	J2000 Coordinates[a]		rms[b] (μK)	t_{int}[c] (min)	ΔT_{SZ}[d] (μK)	$10^{10} \times Y(\theta)$[e]		
		RA	Dec.				$\theta \leq 2'$ (± 0.2)	$\theta \leq 4'$ (± 0.6)	$\theta \leq 6'$ (± 1.1)
ACT-CL J0245–5301	AS0295	$02^h45^m28^s$	$-53°01'36''$	44	10.1	−250	0.93	2.5	4.1
ACT-CL J0330–5228	A3128 (NE)	$03^h30^m50^s$	$-52°28'38''$	49	10.3	−260	0.97	2.8	4.5
ACT-CL J0546–5346	SPT-CL 0547–5345	$05^h46^m35^s$	$-53°46'04''$	46	9.5	−250	0.96	2.5	3.9
ACT-CL J0638–5358	AS0592	$06^h38^m46^s$	$-53°58'40''$	55	7.5	−230	0.74	1.5	2.2
ACT-CL J0658–5556	1E 0657–56 (Bullet)	$06^h58^m33^s$	$-55°56'49''$	80	3.4	−510	1.70	3.20	3.80

[a] Position of the deepest point in 2′ FWHM Gaussian smoothed map.
[b] Map rms measured outside a 6′ mask and reported for a 1 arcmin^2 area.
[c] Integration time, defined as the approximate total time (in minutes) that the telescope was pointed in the map region.
[d] Cluster depth, as measured in a 2′ FWHM Gaussian smoothed map at the listed coordinates; intended as a guide to the magnitude of the decrement.
[e] See Equation (31) and following discussion.

The contribution from noise is readily estimated from the map rms (cf. Sec. 5.1 and Table 2). To estimate the second contribution, we found the standard deviation of Y in the ensemble of simulated, noise-free, primary CMB-only maps described in Section 5.2. This latter source dominates over the error from the map noise. Our estimated 1σ errors, including both sources of uncertainty, are 0.2×10^{-10}, 0.6×10^{-10} and 1.1×10^{-10} for Y at 2′, 4′, and 6′. We arrive at uncertainties that agree to better than 10% by calculating the standard deviation of Y values from the 24 maps of random patches of the sky with no clusters present (cf. Section 5.2).

Uncertainty in the cluster temperature enters into the measurement of Y via the relativistic correction (see above). However, the error introduced is less than a percent and is therefore insignificant in comparison to the contributions from noise and primary CMB anisotropies.

5.4. *Comparisons to Previous Measurements*

The clusters shown in this paper are previously known X-ray, optical, and/or SZ clusters; all are massive systems. For three of the sources (AS0295, A3128 (NE), and AS0592), these are the first reported SZ detections. In this section, we briefly review measurements from the literature to provide context, and point out some of the contributions that our new measurements make to this body of knowledge.

Relevant parameters from the literature are listed in Table 3; references for these values are included below. Typical errors on L_X are small ($< 20\%$), while those on the inferred mass are more substantial ($\sim 50\%$). Temperatures are measured values from X-ray spectra. We use a flat ΛCDM cosmology with $\Omega_M = 0.3$ and $H_0 = 70\,\mathrm{km\,s^{-1}\,Mpc^{-1}}$. Masses are quoted in units of M_{500}, defined as the mass within a radius having a mean mass density $\langle\rho\rangle$ 500 times greater than the critical density, i.e., $\langle\rho\rangle = 500 \times 3H^2/(8\pi G)$. In the following we briefly discuss the clusters in the order in which they appear in Table 2.

5.4.1. *AS0295*

AS0295 first appeared in Abell et al. (1989) in their table of supplementary southern clusters (i.e., clusters that were not rich enough or were too distant to satisfy the criteria for inclusion in the rich nearby cluster catalog). It was also found to be a significant X-ray source in the *ROSAT* All Sky Survey (RASS) Bright Source Catalog (Voges et al. 1999). The spectroscopic redshift of AS0295 was obtained by Edge et al. (1994), who also reported the discovery of a giant strong-lensing arc near the brightest cluster galaxy. Efforts to detect the SZ effect at 1.2 mm

TABLE 3
SUMMARY OF CLUSTER PROPERTIES FROM X-RAY AND OPTICAL STUDIES

ACT Descriptor	Catalog Name	Redshift	D_A [Mpc]	L_X(0.1–2.4 keV) (10^{44} erg s^{-1})	M_{500} ($10^{15} M_\odot$)	kT (keV)	$10^{10} \times Y_{2500}$[a]
ACT-CL J0245–5301	AS0295	0.3006	920	8.3	0.8	6.7 ± 0.7	$0.53^{+0.35}_{-0.21}$
ACT-CL J0330–5228	A3128 (NE)	0.44	1172	3.9	0.3	5.1 ± 0.2	$0.15^{+0.10}_{-0.06}$
ACT-CL J0546–5346	SPT 0547–5345	0.88 (P)	1596	4.7	0.6	—	—
ACT-CL J0638–5358	AS0592	0.2216	737	10.6	1.0	8.0 ± 0.4	$1.31^{+0.86}_{-0.52}$
ACT-CL J0658–5556	1E 0657–56	0.296	910	20.5	1.4	10.6 ± 0.1	$1.61^{+1.16}_{-0.67}$

NOTE. — See Section 5.4 for citations to the literature from which these values were obtained. The marker (P) in the redshift column indicates a photometric redshift measurement.

[a] Predicted value of Y within R_{2500} from the Y-kT scaling relation of Bonamente et al. (2008). Errors come from the uncertainty on the scaling relation parameters. Although we do not have R_{2500} values for our clusters, the $Y(2')$ measurements listed in Table 2 should be roughly comparable to these—see Section 5.4.6.

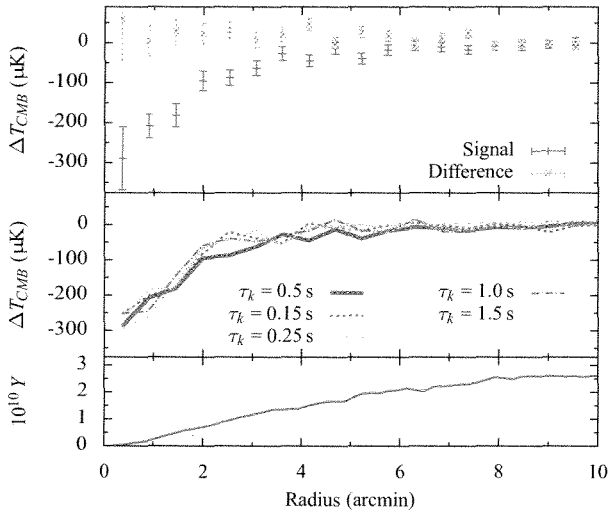

FIG. 8.— The radial profile (top/middle) and integrated Compton $Y(\theta)$ values (bottom) for the SZ decrement of ACT-CL J0638–5358 (AS0592). The profile data are averages from the maps in 32″ wide annuli, and $Y(\theta)$ is the sum of the pixels within a radius θ, converted to the unitless Compton-y parameter (Equations (29) and (31)). The top panel shows the profile of the signal map and difference map. The middle panel compares profiles for maps made with different knot spacings τ_k, showing that the choice of knot spacing does not significantly bias the measured cluster profile. In all of the panels, the profile centers were determined by the minimum of the map after smoothing with a 2′ FWHM Gaussian profile. (The profiles were calculated from the unsmoothed maps.)

and 2 mm with the Swedish-ESO Submillimetre Telescope were attempted, unsuccessfully, by Andreani et al. (1996). *ASCA* observations (Fukazawa et al. 2004) yielded values (see Table 3) for average temperature and soft band X-ray flux(0.1–2.4 keV), from which we determined the corresponding X-ray luminosity. The cluster mass M_{500} was then estimated from the luminosity-mass (specifically L_X(0.1-2.4 keV) versus M_{500}) relations from Reiprich & Böhringer (2002).

5.4.2. *A3128 (NE)*

Until quite recently the north-east (NE) component of A3128 was believed to be part of the Horologium-Reticulum supercluster at $z = 0.06$. The X-ray morphology is clearly double peaked with the two components separated on the sky by some 12′. Rose et al. (2002) estimated the virial masses of the two components assuming the redshift of the supercluster and obtained a value for each of $\sim 1.5 \times 10^{14} M_\odot$. Figure 9 shows our SZ measurement with overlaid X-ray contours.

Recently Werner et al. (2007) carried out a detailed study of this cluster using *XMM-Newton* data, which revealed a more distant and more massive cluster superposed on the northeastern component of A3128. A significant portion of the X-ray emission comes from this background cluster. The values we quote in the table for redshift, X-ray luminosity, gas temperature, and M_{500} correspond to the background cluster and come from Werner et al. (2007).

The large SZ decrement seen in the ACT maps is clearly associated with the NE component where the $z = 0.44$ cluster is. We do not detect a significant decrement from the southwestern component which lies at $z = 0.06$. Werner et al. (2007) estimate the temperature of the higher redshift cluster to be 5.14 ± 0.15 keV, which is significantly hotter than that of the foreground cluster ($kT = 3.36 \pm 0.04$ keV). This system, therefore, is a compelling illustration of the mass selection, approximately independent of redshift, of the SZ effect. Werner et al. (2007) note that the temperature, luminosity, and mass estimates of the $z = 0.44$ background cluster are all subject to large systematic errors, as the cluster properties depend upon the assumed properties of the foreground system. A joint X-ray/SZ/optical analysis should be able to better constrain the characteristics of both systems and thereby contribute to assessing the mass threshold of the ACT cluster survey.

5.4.3. *SPT 0547–5345*

The galaxy cluster SPT 0547–5345 was first discovered via the SZ effect by the South Pole Telescope (Staniszewski et al. 2009). Its physical properties—photometric redshift, luminosity, temperature and mass estimate—were subsequently reported by Menanteau & Hughes (2009) based on optical and X-ray data.

SPT 0547–5345 has associated central elliptical galaxies with luminosities consistent with those of clusters in the Sloan Digital Sky Survey. Its mass estimate from the optical and X-ray luminosity also suggests that it is a fairly massive system. In Table 3 we list its M_{500} estimates from the X-ray luminosity.

5.4.4. *AS0592*

The galaxy cluster AS0592 was originally detected optically (Abell et al. 1989). *ROSAT* detected it as a bright source in the All Sky Survey and its redshift ($z = 0.2216$) was reported in de Grandi et al. (1999). The cluster is also known by its REFLEX designation of RXC J0638.7–5358 (Böhringer et al. 2004). The *ROSAT* flux and luminosity in the soft X-ray band (0.1-2.4 keV) are 7.5×10^{-12} erg cm^{-2} s^{-1} and 1.1×10^{45} ergs s^{-1}. The X-ray spectrum of AS0592 from a *Chandra* observation (Hughes et al. 2009) yields an integrated gas temperature of

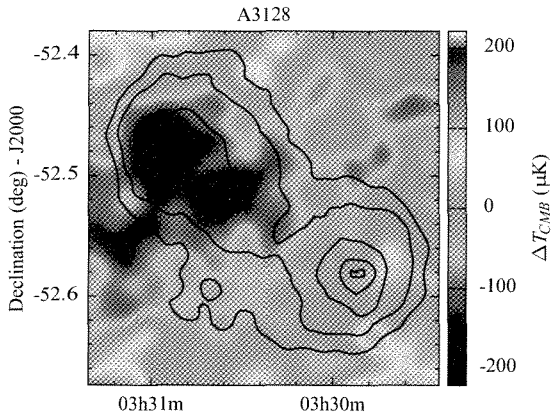

FIG. 9.— ACT-CL J0330-5228 (A3128 (NE)) with overlaid contours of X-ray emission in black. The SZ detection is associated with the NE feature of A3128, and confirms that it is due to a more massive, higher redshift cluster than that at the SW lobe—a compelling example of the redshift independent mass selection of the SZ effect. The X-ray data come from two separate *XMM-Newton* observations (Obs Ids 0400130101 and 0400130201) with a total exposure time of 104 ks. The two observations were mosaicked into a single image over the 0.2–2.0 keV. Contour values are from 1.25×10^{-8} to 1.25×10^{-7} photons cm^{-2} s^{-1} arcsec^{-2}.

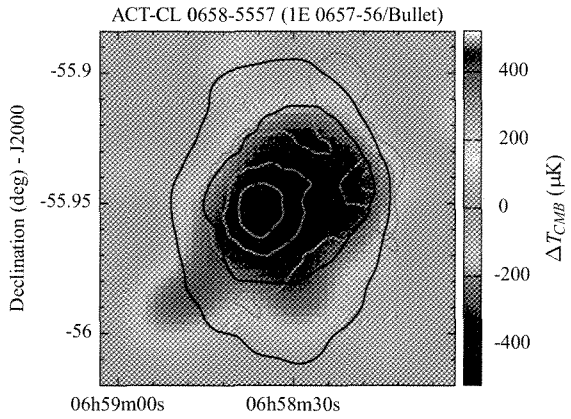

FIG. 10.— ACT-CL J0658-5556 (Bullet Cluster) with overlaid contours of X-ray emission (black) and dark matter distribution (orange). The X-ray contours come from an 85 ks-long *Chandra* observation (Obs Id 3184) and correspond to the 0.5-2.0 keV band. Contour values are 4×10^{-7} to 2×10^{-9} photons cm^{-2} s^{-1} arcsec^{-2}. The lensing data are from Clowe et al. (2007) with contours running from $\kappa = 0.12$ to 0.39.

$kT = 8.0 \pm 0.4$ keV. The soft X-ray luminosity implies a cluster mass of $M_{500} = 10^{15} M_{\odot}$.

5.4.5. *1E 0657–56 (Bullet Cluster)*

We detect 1E 0657–56, the famous "Bullet" cluster, at high significance with a strong central decrement and large integrated Y. Previous detections of the millimeter-band SZ signal from this cluster have been reported by ACBAR (Gomez et al. 2004) and APEX-SZ (Halverson et al. 2008).

The spectroscopic redshift of 1E 0657–56 was obtained by Tucker et al. (1998), the X-ray flux came from the Einstein Observatory (Markevitch et al. 2002), the X-ray gas temperature from *XMM-Newton* (Zhang et al. 2006), and the cluster mass, M_{500}, from a study by Zhang et al. (2008).

Figure 10 shows a zoomed-in plot of our SZ map with X-ray contours from *Chandra* and lensing contours from Clowe et al. (2007). As expected, the SZ decrement follows the X-ray contours more closely than the lensing contours, since the collisionless dark matter is expected to be offset from the collisional gas in this merging system.

5.4.6. *Comparison with Previous SZ Measurements*

Although the large masses of the ACT-detected clusters we report here offer strong support for the reality of our detections, we also compare the quoted integrated Compton-y parameters for consistency with expectations from previous SZ cluster studies. For this we use the Y-kT scaling relation from Bonamente et al. (2008) (using values for "all clusters" from their Table 2). Predicted values are given in the last column of Table 3. The Y values in the scaling relation were integrated within R_{2500}, the radius where the average cluster mass density is 2500 times the critical density. We do not have precise R_{2500} values for our clusters, but estimates of R_{2500} range from about $1'$ to $3'$, so the predicted values of $Y(2500)$ should, to first order, be roughly comparable to our $Y(2')$ values. With that proviso, the predicted and measured Y values agree to within 2σ for all clusters except A3128 (NE), where the cluster temperature predicts a much lower Y value than we measure. Since it is a complex system, it could have a larger mass than previously thought. A larger and better-studied sample of ACT-detected clusters will be necessary before drawing conclusions about scaling relations.

6. CONCLUSIONS

In this paper we have presented beam maps and SZ cluster measurements from the first full season of 148 GHz data from ACT. They represent the first scientific results from ACT and demonstrate that it is poised to make important contributions to millimeter astronomy.

We have described a maximum-likelihood mapping algorithm which uses B-splines to model atmospheric signal and to remove it from the data. The method has been used to make high precision (< -40 dB) beam maps, with solid angles in the 148 GHz, 218 GHz, and 277 GHz bands of (218.2 ± 4) nsr, (118.2 ± 3) nsr, and (104.2 ± 6) nsr, respectively. The beam profiles and window functions will be important for all subsequent analyses of ACT's data.

Additionally, we have made maps showing SZ decrements of five previously discovered galaxy clusters. Of these, three are detected for the first time via the SZ effect. Our high-significance detection of the $z = 0.44$ component of A3128, and our current non-detection of the low-redshift part, corroborates existing evidence that the further cluster is more massive. This is a compelling example of the redshift-independent mass selection of the SZ effect which will be exploited in future studies of ACT clusters.

A preprint of this paper included three additional clusters: ACT-CL J0509–5345, ACT-CL J0516–5432, and ACT-CL J0645–5413. They are instead quantified in Menanteau et al. (2010) and Marriage et al. (2010). We omitted them here in order to focus on the more significant of the initial ACT cluster detections.

The ACT project was proposed in 2000 and funded 2004 Jan 1. Many have contributed to the project since its inception. We especially wish to thank Asad Aboobaker, Christine Allen, Dominic Benford, Paul Bode, Kristen Burgess, Angelica de Oliveria-Costa, Peter Hargrave, Norm Jarosik, Amber Miller, Carl Reintsema, Uros Seljak, Martin Spergel, Johannes Staghun, Carl Stahle, Max Tegmark, Masao Uehara, and Ed Wishnow. It is a pleasure to acknowledge Bob Margolis,

ACT's project manager. Reed Plimpton and David Jacobson worked at the telescope during the 2008 season. ACT is on the Chajnantor Science preserve which was made possible by CONICYT. We are grateful for the assistance we received at various times from the ALMA, APEX, ASTE, CBI/QUIET, and NANTEN2 groups. The PWV data come from the public APEX weather site. Field operations were based at the Don Esteban facility run by Astro-Norte. This research has made use of the NASA/IPAC Extragalactic Database (NED) which is operated by the Jet Propulsion Laboratory, California Institute of Technology, under contract with the National Aeronautics and Space Administration. Satoshi Nozawa and Naoki Itoh kindly shared their code for calculating relativistic corrections to the SZ effect. We also thank William Holzapfel and an anonymous referee who provided helpful feedback on an earlier version of this paper. We thank the members of our external advisory board—Tom Herbig (chair), Charles Alcock, Walter Gear, Cliff Jackson, Amy Newbury, and Paul Steinhardt—who helped guide the project to fruition. This work was supported by the U.S. National Science Foundation through awards AST-0408698 for the ACT project, and PHY-0355328, AST-0707731 and PIRE-0507768. Funding was also provided by Princeton University and the University of Pennsylvania. A.D.H. received additional support from a Natural Science and Engineering Research Council of Canada (NSERC) PGS-D scholarship. A.K. and B.P. were partially supported through NSF AST-0546035 and AST-0606975, respectively, for work on ACT. H.Q. and L.I. acknowledge partial support from FONDAP Centro de Astrofisica. E.S. acknowledges support by NSF Physics Frontier Center grant PHY-0114422 to the Kavli Institute of Cosmological Physics. K.M., M.H., and R.W. received financial support from the South African National Research Foundation (NRF), the Meraka Institute via funding for the South African Centre for High Performance Computing (CHPC), and the South African Square Kilometer Array (SKA) Project. R.H. received funding from the Rhodes Trust. L.V. acknowledges support from NSF-AST 0707731 and FP7-PEOPLE-2007-4-3 IRG no. 202182. J.B.J. acknowledges for support from FONDECYT (no: 3085031).

APPENDIX

A. THE COTTINGHAM METHOD AS A MAXIMUM-LIKELIHOOD ESTIMATOR

Equation (1) can be written in the matrix form,

$$d = \begin{pmatrix} \mathbf{P} & \mathbf{B} \end{pmatrix} \begin{pmatrix} m \\ \alpha \end{pmatrix} + n, \tag{A1}$$

which has the maximum-likelihood estimator:

$$\begin{pmatrix} \widetilde{m} \\ \widetilde{\alpha} \end{pmatrix} = \left[\begin{pmatrix} \mathbf{P}^T \\ \mathbf{B}^T \end{pmatrix} \mathbf{N}^{-1} \begin{pmatrix} \mathbf{P} & \mathbf{B} \end{pmatrix} \right]^{-1} \begin{pmatrix} \mathbf{P}^T \\ \mathbf{B}^T \end{pmatrix} \mathbf{N}^{-1} d = \begin{bmatrix} (\mathbf{PP}) & (\mathbf{PB}) \\ (\mathbf{BP}) & (\mathbf{BB}) \end{bmatrix}^{-1} \begin{pmatrix} \mathbf{P}^T\mathbf{N}^{-1}d \\ \mathbf{B}^T\mathbf{N}^{-1}d \end{pmatrix}, \tag{A2}$$

where we use the shorthand notation $(\mathbf{XY}) \equiv \mathbf{X}^T\mathbf{N}^{-1}\mathbf{Y}$. The inverted matrix evaluates to:

$$\begin{bmatrix} \left[(\mathbf{PP}) - (\mathbf{PB})(\mathbf{BB})^{-1}(\mathbf{BP})\right]^{-1} & -(\mathbf{PP})^{-1}(\mathbf{PB})\left[(\mathbf{BB}) - (\mathbf{BP})(\mathbf{PP})^{-1}(\mathbf{PB})\right]^{-1} \\ -(\mathbf{BB})^{-1}(\mathbf{BP})\left[(\mathbf{PP}) - (\mathbf{PB})(\mathbf{BB})^{-1}(\mathbf{BP})\right]^{-1} & \left[(\mathbf{BB}) - (\mathbf{BP})(\mathbf{PP})^{-1}(\mathbf{PB})\right]^{-1} \end{bmatrix}. \tag{A3}$$

Since this matrix is symmetric, and $(\mathbf{XY})^T = (\mathbf{YX})$, we can rewrite the lower-left component as:

$$(\mathbf{BB})^{-1}(\mathbf{BP})\left[(\mathbf{PP}) - (\mathbf{PB})(\mathbf{BB})^{-1}(\mathbf{BP})\right]^{-1} = \left\{(\mathbf{PP})^{-1}(\mathbf{PB})\left[(\mathbf{BB}) - (\mathbf{BP})(\mathbf{PP})^{-1}(\mathbf{PB})\right]^{-1}\right\}^T \tag{A4}$$

$$= \left[(\mathbf{BB}) - (\mathbf{BP})(\mathbf{PP})^{-1}(\mathbf{PB})\right]^{-1}(\mathbf{BP})(\mathbf{PP})^{-1}. \tag{A5}$$

Thus, the solution for the atmosphere is:

$$\widetilde{\alpha} = \left[(\mathbf{BB}) - (\mathbf{BP})(\mathbf{PP})^{-1}(\mathbf{PB})\right]^{-1}\mathbf{B}^T\mathbf{N}^{-1}d - \left[(\mathbf{BB}) - (\mathbf{BP})(\mathbf{PP})^{-1}(\mathbf{PB})\right]^{-1}(\mathbf{BP})(\mathbf{PP})^{-1}\mathbf{P}^T\mathbf{N}^{-1}d. \tag{A6}$$

To show that this is equivalent to the solution presented in Section 2.1, we observe that the definitions in Equations (3) and (6) of Section 2.1 can be recast:

$$\begin{aligned} \Theta \equiv \mathbf{B}^T\mathbf{N}^{-1}(\mathbf{1} - \mathbf{P}\Pi)\mathbf{B} &= (\mathbf{BB}) - (\mathbf{BP})(\mathbf{PP})^{-1}(\mathbf{PB}), \\ \phi \equiv \mathbf{B}^T\mathbf{N}^{-1}(\mathbf{1} - \mathbf{P}\Pi)d &= \left[\mathbf{B}^T\mathbf{N}^{-1} - (\mathbf{BP})(\mathbf{PP})^{-1}\mathbf{P}^T\mathbf{N}^{-1}\right]d. \end{aligned} \tag{A7}$$

This reduces Equation (A6) to:

$$\widetilde{\alpha} = \Theta^{-1}\phi, \tag{A8}$$

which is the same as Equation (7) of Section 2.1.

B. A PLANET'S SOLID ANGLE CONTRIBUTION TO THE BEAM SOLID ANGLE MEASUREMENT

Denote the instrument response with $P(n)$ and the power emitted by the planet with $P_0\Psi(n)$, where P_0 is the peak power emitted and Ψ is a normalized distribution describing its shape. The coordinate n is a two dimensional vector describing the position on the sky, with $n = 0$ at the planet center. The measured beam map, $\widetilde{B}$, is the convolution of the true beam, B, with the planet:

$$\widetilde{B}(n) = \frac{P(n)}{P(0)} = \frac{\iint d\Omega_{n'} B(n-n')\Psi(n')}{\iint d\Omega_{n'} B(-n')\Psi(n')}. \tag{B1}$$

The measured solid angle is then (cf. Equation (13)):

$$\widetilde{\Omega}_A = \iint d\Omega_n \frac{\iint d\Omega_{n'} B(n-n')\Psi(n')}{\iint d\Omega_{n'} B(-n')\Psi(n')} = \frac{\left[\iint d\Omega_{n'}\Psi(n')\right]\left[\iint d\Omega_n B(n)\right]}{\iint d\Omega_{n'} B(n')\Psi(n')} = \frac{\Omega_\Psi \Omega_A}{\iint d\Omega_{n'} B(n')\Psi(n')}, \tag{B2}$$

where in the second equality we brought the denominator outside the outer integral, and in the numerator we switched the order of integration and then shifted the dummy variable for the integral over B. In the last equality we recognized that the integrals in the numerator evaluate to the solid angles of the planet and the true instrument beam, respectively. If the planet is much smaller than the beam, we can expand the beam appearing the integrand of the denominator in a Taylor series:

$$B(n) = 1 + \nabla B(0)\cdot n + \frac{1}{2} n\cdot \mathbf{H}(0)\cdot n + \cdots, \tag{B3}$$

where $\mathbf{H}$ is the Hessian matrix of the beam. At the beam center, being the peak, the gradient vanishes. If we assume a symmetric beam, then $n\cdot\mathbf{H}\cdot n = (\nabla^2 B/2)|n|^2$, and we can write:

$$\widetilde{\Omega}_A \approx \frac{\Omega_\Psi \Omega_A}{\iint d\Omega_{n'}\left[1+\frac{1}{4}\nabla^2 B(0)|n'|^2\right]\Psi(n')} = \Omega_A\left[1+\frac{\nabla^2 B(0)}{4\Omega_\Psi}\iint d\Omega_{n'}|n'|^2\Psi(n')\right]^{-1} = \Omega_A\left[1+\frac{\nabla^2 B(0)}{4\Omega_\Psi}\mu_2^\Psi\right]^{-1}, \tag{B4}$$

where μ_2^Ψ is the second raw moment of the planet shape Ψ. In the small planet approximation we are making, the second term in the brackets is small. Thus:

$$\widetilde{\Omega}_A \approx \Omega_A - \frac{\Omega_A}{\Omega_\Psi}\frac{\nabla^2 B(0)}{4}\mu_2^\Psi. \tag{B5}$$

For a disk, $\mu_2^\Psi = \Omega_\Psi^2/2\pi$, and both a Gaussian beam and an Airy pattern have $\nabla^2 B(0) = -4\pi/\Omega_A$. (For the Airy pattern, this is easiest to see by expanding the Bessel function in a power series and differentiating.) Thus, we have the result that $\widetilde{\Omega}_A \approx \Omega_A + \Omega_\Psi/2$.

REFERENCES

Abell, G. O., Corwin, Jr., H. G., & Olowin, R. P. 1989, ApJS, 70, 1
Andreani, P. et al. 1996, ApJ, 459, L49, arXiv:astro-ph/9602011
Battistelli, E. S. et al. 2008, in Proc. SPIE, ed. W. D. Duncan, W. S. Holland, S. Withington, & J. Zmuidzinas, Vol. 7020 (SPIE), 702028
Benson, B. A., Church, S. E., Ade, P. A. R., Bock, J. J., Ganga, K. M., Henson, C. N., & Thompson, K. L. 2004, ApJ, 617, 829, arXiv:astro-ph/0404391
Böhringer, H. et al. 2004, A&A, 425, 367, arXiv:astro-ph/0405546
Bojanov, B. D., Hakopian, H. A., & Sahakian, A. A. 1993, Spline Functions and Multivariate Interpolations (Kluwer Academic Publishers)
Bonamente, M., Joy, M., LaRoque, S. J., Carlstrom, J. E., Nagai, D., & Marrone, D. P. 2008, ApJ, 675, 106, 0708.0815
Bond, J. R. 1996, in Cosmology and Large Scale Structure, ed. R. Schaeffer, J. Silk, M. Spiro, & J. Zinn-Justin, 469
Born, M., & Wolf, E. 1999, Principles of Optics, 7th edn. (Cambridge University Press)
Boughn, S. P., Cheng, E. S., Cottingham, D. A., & Fixsen, D. J. 1992, ApJ, 391, L49
Burigana, C., Malaspina, M., Mandolesi, N., Danse, L., Maino, D., Bersanelli, M., & Maltoni, M. 1999, Internal Report ITESRE 198/1997, arXiv:astro-ph/9906360
Clowe, D., Randall, S. W., & Markevitch, M. 2007, Nuclear Physics B Proceedings Supplements, 173, 28, arXiv:astro-ph/0611496
Cottingham, D. A. 1987, PhD thesis, Princeton University
de Boor, C. 2001, A Practical Guide to Splines, revised edn. (Springer)
de Grandi, S. et al. 1999, ApJ, 514, 148, arXiv:astro-ph/9902067
Delabrouille, J. 1998, A&AS, 127, 555
Edge, A. C. et al. 1994, A&A, 289, L34, arXiv:astro-ph/9407078
Fowler, J. W. et al. 2007, Appl. Opt., 46, 3444
Friedman, R. B. et al. 2009, ApJ, 700, L187, 0901.4334
Fukazawa, Y., Makishima, K., & Ohashi, T. 2004, PASJ, 56, 965, arXiv:astro-ph/0411745
Ganga, K., Cheng, E., Meyer, S., & Page, L. 1993, ApJ, 410, L57
Gomez, P. et al. 2004, in American Institute of Physics Conference Series, Vol. 703, Plasmas in the Laboratory and in the Universe: New Insights and New Challenges, ed. G. Bertin, D. Farina, & R. Pozzoli, 361–366
Griffin, M. J., & Orton, G. S. 1993, Icarus, 105, 537
Halverson, N. W. et al. 2008, arXiv:0807:4208, 0807.4208
Hincks, A. D. et al. 2008, in Proc. SPIE, ed. W. D. Duncan, W. S. Holland, S. Withington, & J. Zmuidzinas, Vol. 7020 (SPIE), 70201P
Hinshaw, G. et al. 2007, ApJS, 170, 288, arXiv:astro-ph/0603451
Hughes, J. P., Menanteau, F., Sehgal, N., Infante, L., & Barrientos, F. 2009, in Bulletin of the American Astronomical Society, Vol. 41, Bulletin of the American Astronomical Society, 336
Keihänen, E., Kurki-Suonio, H., & Poutanen, T. 2005, MNRAS, 360, 390, arXiv:astro-ph/0412517
Keihänen, E., Kurki-Suonio, H., Poutanen, T., Maino, D., & Burigana, C. 2004, A&A, 428, 287, arXiv:astro-ph/0304411
Komatsu, E., & Seljak, U. 2001, MNRAS, 327, 1353
Kramer, C., Moreno, R., & Greve, A. 2008, A&A, 482, 359, 0801.4452
Kuo, C. L. et al. 2004, ApJ, 600, 32, arXiv:astro-ph/0212289
Maino, D., Burigana, C., Górski, K. M., Mandolesi, N., & Bersanelli, M. 2002, A&A, 387, 356, arXiv:astro-ph/0202271
Markevitch, M., Gonzalez, A. H., David, L., Vikhlinin, A., Murray, S., Forman, W., Jones, C., & Tucker, W. 2002, ApJ, 567, L27, arXiv:astro-ph/0110468
Marriage, T. A. et al. 2010, ArXiv e-prints, 1010.1065
Marriage, T. A., Chervenak, J. A., & Doriese, W. B. 2006, Nuc Inst & Meth. in Phys Res A, 559, 551
Marten, A., Matthews, H. E., Owen, T., Moreno, R., Hidayat, T., & Biraud, Y. 2005, A&A, 429, 1097
Menanteau, F. et al. 2010, ApJ, 723, 1523, 1006.5126
Menanteau, F., & Hughes, J. P. 2009, ApJ, 694, L136, 0811.3596
Meyer, S. S., Cheng, E. S., & Page, L. A. 1991, ApJ, 371, L7
Niemack, M. D. 2006, in Presented at the Society of Photo-Optical Instrumentation Engineers (SPIE) Conference, Vol. 6275, Society of Photo-Optical Instrumentation Engineers (SPIE) Conference Series, 62750C

Niemack, M. D. et al. 2008, J. Low Temp. Phys., 151, 690
Nozawa, S., Itoh, N., Suda, Y., & Ohhata, Y. 2006, Nuovo Cimento B Serie, 121, 487, arXiv:astro-ph/0507466
Page, L. et al. 2003, ApJS, 148, 39, arXiv:astro-ph/0302214
Pérez-Beaupuits, J. P., Rivera, R. C., & Nyman, L.-A. 2005, Height and Velocity of the Turbulence Layer at Chajnantor Estimated From Radiometric Measurements, Memo 542, Atacama Large Millimeter Array (ALMA, Charlottesville, VA: NRAO)
Press, W. H., Teukolsky, S. A., Vetterling, W. T., & Flannery, B. P. 1992, Numerical Recipes in C: The Art of Scientific Computing, 2nd edn. (Cambridge University Press)
Reichardt, C. L. et al. 2009a, ApJ, 694, 1200, 0801.1491
——. 2009b, ApJ, 701, 1958, 0904.3939
Reiprich, T. H., & Böhringer, H. 2002, ApJ, 567, 716, arXiv:astro-ph/0111285
Rephaeli, Y. 1995, ApJ, 445, 33
Rose, J. A., Gaba, A. E., Christiansen, W. A., Davis, D. S., Caldwell, N., Hunstead, R. W., & Johnston-Hollitt, M. 2002, AJ, 123, 1216, arXiv:astro-ph/0112346
Schroeder, D. J. 2000, Astronomical Optics, 2nd edn. (Academic Press)
Schumaker, L. L. 2007, Spline Functions: Basic Theory, 3rd edn. (Cambridge University Press)
Sharp, M. K. et al. 2010, ApJ, 713, 82, 0901.4342
Sievers, J. L. et al. 2009, arXiv:0901.4540, 0901.4540
Staniszewski, Z. et al. 2009, ApJ, 701, 32, 0810.1578
Sunyaev, R. A., & Zel'dovich, Y. B. 1970, Comments on Astrophysics and Space Physics, 2, 66
Sutton, D., Johnson, B. R., Brown, M. L., Cabella, P., Ferreira, P. G., & Smith, K. M. 2009, MNRAS, 393, 894, 0807.3658
Swetz, D. S. et al. 2008, in Proc. SPIE, ed. W. D. Duncan, W. S. Holland, S. Withington, & J. Zmuidzinas, Vol. 7020 (SPIE), 702008
Switzer, E. R. et al. 2008, in Proc. SPIE, ed. A. Bridger & N. M. Radziwill, Vol. 7019 (SPIE), 70192L
Tegmark, M. 1997, ApJ, 480, L87, arXiv:astro-ph/9611130
Thornton, R. J. et al. 2008, in Proc. SPIE, ed. W. D. Duncan, W. S. Holland, S. Withington, & J. Zmuidzinas, Vol. 7020 (SPIE), 70201R
Tucker, W. et al. 1998, ApJ, 496, L5, arXiv:astro-ph/9801120
Umetsu, K. et al. 2009, ApJ, 694, 1643, 0810.0969
Verde, L., Haiman, Z., & Spergel, D. N. 2002, ApJ, 581, 5, arXiv:astro-ph/0106315
Voges, W. et al. 1999, A&A, 349, 389, arXiv:astro-ph/9909315
Werner, N., Churazov, E., Finoguenov, A., Markevitch, M., Burenin, R., Kaastra, J. S., & Böhringer, H. 2007, A&A, 474, 707, 0708.3253
White, M., & Srednicki, M. 1995, ApJ, 443, 6, arXiv:astro-ph/9402037
Zeldovich, Y. B., & Sunyaev, R. A. 1969, Ap&SS, 4, 301
Zhang, Y.-Y., Böhringer, H., Finoguenov, A., Ikebe, Y., Matsushita, K., Schuecker, P., Guzzo, L., & Collins, C. A. 2006, A&A, 456, 55, arXiv:astro-ph/0603275
Zhang, Y.-Y., Finoguenov, A., Böhringer, H., Kneib, J.-P., Smith, G. P., Kneissl, R., Okabe, N., & Dahle, H. 2008, A&A, 482, 451, 0802.0770
Zhao, Y. et al. 2008, in Proc. SPIE, ed. W. D. Duncan, W. S. Holland, S. Withington, & J. Zmuidzinas, Vol. 7020 (SPIE), 70200O